CLIC Note 627

# UPDATED CLIC PARAMETERS 2005

H. Braun, R. Corsini, A. De Roeck, A. Grudiev, S. Heikkinen, E. Jensen, M. Korostelev, D. Schulte, I. Syratchev,
F. Tecker (editor), W. Wunsch, F. Zimmermann, CERN, Geneva

for the CLIC study team

## Abstract

This note presents the CLIC parameter set as of mid 2005 and describes the different sub-systems, stressing how the design of the different components is driven.

This design emerged from a better understanding of limitations for normal conducting accelerating structures, which led to a new optimised design for the CLIC 30 GHz accelerating structure. The structure parameters and improvements in other sub-systems have resulted in a major revision of the parameters. The overall layout and efficiencies for CLIC with this updated parameter-set are presented.

Geneva, Switzerland
May 12, 2006

# Contents

# 1 Overview and Rationale

Substantial progress has been made during the last years in the understanding of field and pulse length limitations in normal conducting accelerating structures. A large amount of data has been provided by the X-band tests in NLCTA and the Ka-band experiments in CTF II. Other studies have addressed problems of material fatigue related to pulsed heating and plasma dynamics of breakdowns [1]. In parallel with these developments, the understanding of low emittance generation in damping rings and emittance preservation during beam transport through the main linac and the beam delivery system has improved, and the dependency of luminosity on beam parameters has been studied in detail [2].

In the light of these new results it became apparent that the old CLIC main beam accelerating structure design TDS [3] would not be able to operate with the accelerating gradient and pulse length as published in [4]. This triggered the development of a new accelerating structure concept named HDS (Hybrid Damped Structure) [5]. Since RF breakdown is not well understood and therefore difficult to predict, extrapolations from available data have been used for the HDS as design guidelines, to impose limits on surface field strengths, power flow and pulse length. While the HDS has a significantly improved damping of long range wake-potentials, the short range wake-potential is increased due to a reduced aperture. In order to keep the emittance growth in the main linac under control, this necessitates a reduction of bunch charge, while the improved damping allows the distance between bunches to be decreased. Although the HDS design has significantly reduced surface fields compared with the TDS, the pulsed surface heating for a RF pulse length of 130 ns as assumed in the previous parameters was still unacceptably high and required a reduction of RF pulse length by roughly a factor of two.

Taking all this into account necessitates a major review and adaptation of the CLIC parameters and subsystem designs to bring the parameters into line with the recent developments. The goals for these new parameters are

- Produce a set of parameters giving the best overall physics performance, consistent with our present knowledge of limitations.
- Produce consistent guidelines/specifications for the design of CLIC components.
- Produce consistent guidelines/specifications for feasibility demonstrations in the CLIC test facilities.

As a specification given by physics requirements [6] we assume the same centre-of-mass (CMS) energy $E_{\text{CMS}}$ of 3 TeV and at least the same luminosity $\mathcal{L}_1$ in a 1% energy bin ($\mathcal{L}_1 = 3.3 \cdot 10^{34} \text{ cm}^{-2} s^{-1}$). For this revision of the parameter set we decided to keep the following key parameters fixed although these may also be modified in the future after further studies:

- Loaded accelerating gradient $G = 150\,\text{MV/m}$.
- Main linac RF frequency $f_{\text{rf}} = 30\,\text{GHz}$.

The figure of merit used in the optimisation is the Luminosity in a 1% energy bin divided by the mains power. This was chosen because it facilitates the optimisation process compared with a more refined criterium like luminosity divided by total cost (=investment and running costs over some assumed lifetime of the collider). Figure 1 shows a schematic of the process used to derive the parameters.

Although the improvements in the design of the accelerating structure are the main driving force for the parameter changes, substantial changes have also been made to many subsystems, in particular the damping rings, the power extraction and transfer structures (PETS) and the drive beam generation complex. These changes reflect recent improvements in the systems as well as the modification of beam parameters resulting from the changes in the accelerating structure. We did not consider details of the injector chain upstream of the damping rings, but provide a specification for the beam parameters to be delivered to the damping rings (see section 5). The reasoning for this simplification is that no major feasibility issues are expected from this part of the accelerator complex.

One shortfall of these new parameters should be kept in mind. We were not able to find a working point in a regime for which the $\mathcal{L} \sim P_{\text{beam}}/\sqrt{\sigma_z}$ scaling of [7] is valid. This would require either a higher bunch charge or a smaller horizontal spot size in the IP [8]. Working in this regime would allow for more favorable parameters, but would require either a reduction of short range wake fields in the accelerating structures or substantial progress on low emittance generation and transport.

It should be kept in mind that the optimisation depends strongly on different RF constraints that are not precisely known and that are under further investigation. Different criteria that might evolve in the future could change the parameters significantly. This note presents a consistent set of the parameters with the constraints as of mid 2005.

After a short recapitulation of the physics requirements in the following section, the new HDS accelerating structure and its optimisation process are presented in section 3. The lower bunch charge required for this structure drives the new damping ring parameters that are shown in section 4. The main linac beam transport, the beam delivery system and the interaction point are described in the following sections 6 and 7. Section 8 explains the two-beam module layout for the main linac and the power generating PETS structure. The shorter RF pulse length has substantial implications on the drive beam generation complex which is shown in section 9. The overall layout, power efficiencies and the power consumption are illustrated in section 10 for the 3 TeV design. Finally, section 11 presents possible parameters at 1 TeV, which can be a first stage of a later 3 TeV CLIC.
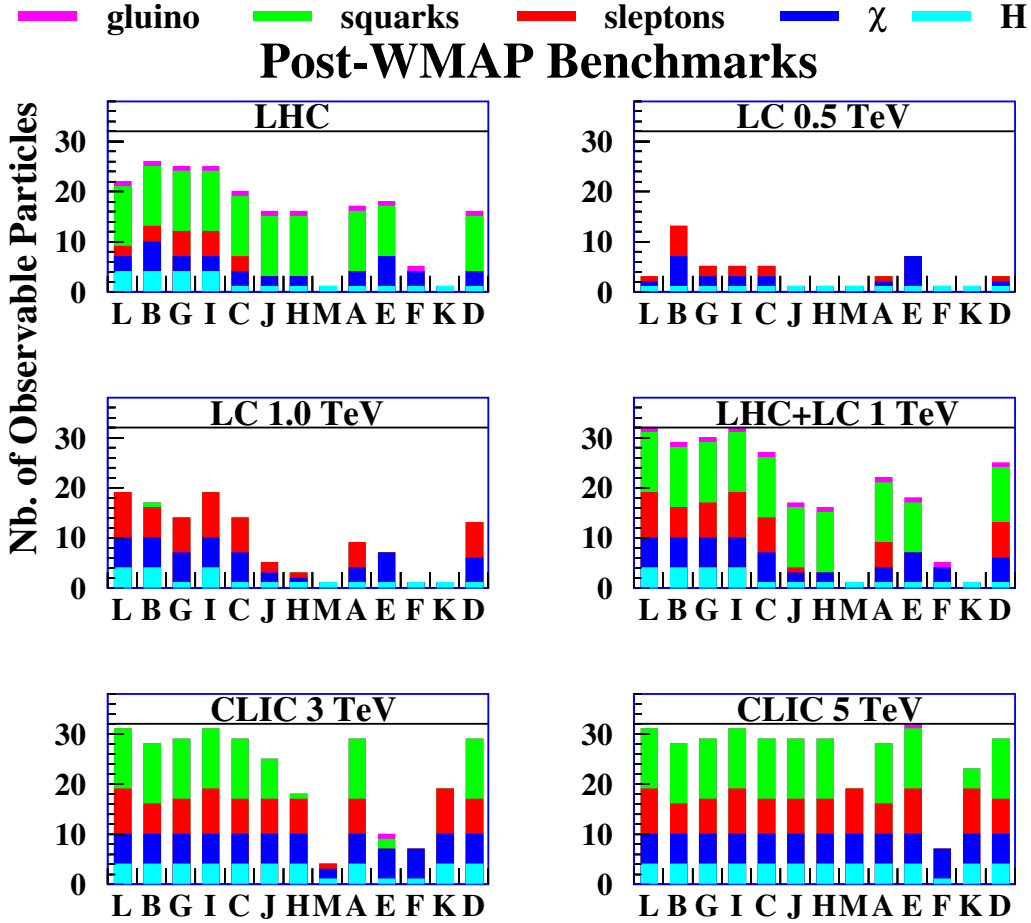
Figure 1: Flow chart of parameter interdependence.

## 2 Physics Requirements

The next energy frontier in High Energy Physics is in the range up to 1 TeV, which will first be explored by the LHC. Just as $e^+e^-$ colliders provided an essential complement to hadron–hadron colliders in the 100 GeV energy range, establishing beyond doubt the validity of the Standard Model, so we expect that higher-energy $e^+e^-$ colliders will be needed to help unravel the TeV physics, to be unveiled by the LHC. They provide very clean experimental environments and democratic production of all particles within the accessible energy range, including those with only electroweak interactions. These considerations motivate several projects for $e^+e^-$ future colliders. The collider considered in this report has the so far unique feature that it aims for $e^+e^-$ centre of mass energies of up to 3-5 TeV, at high luminosities.

The best candidate for new physics at the TeV scale is that associated with generating masses for elementary particles. This is expected to involve a Higgs boson, or something to replace it. The precision electroweak data from LEP and elsewhere rule out many alternatives to the single elementary Higgs boson predicted by the Standard Model, and suggest that it should weigh $\lesssim 200$ GeV. A single elementary Higgs boson is not thought to be sufficient by itself to explain the variety of the different mass scales in physics. Many theories beyond the Standard Model, such as those postulating supersymmetry, extra dimensions or new strong interactions, predict the appearance of non-trivial new dynamics at the TeV scale.

For example, supersymmetry predicts that every particle in the Standard Model should be accompanied by a super-symmetric partner weighing $\lesssim 1$ TeV. Alternatively, theories with extra spatial dimensions predict the appearance of new particle excitations or other structural phenomena at the TeV scale. Finally, alternatives to an elementary Higgs boson, such as new strong interactions, also predict many composite resonances and other effects observable at the TeV energy scale.

Whilst there is no direct evidence, there are various indirect experimental hints that there is indeed new dynamics at the TeV scale. One is the above-mentioned agreement of precision electroweak data with the Standard Model, *if* there is a relatively light Higgs boson. Another is the agreement of the gauge couplings measured at LEP and elsewhere with the predictions of simple grand unified theories, *if* there is a threshold for new physics at the TeV scale, such as supersymmetry. Another hint may be provided by the apparent dominance of dark matter in

2

Figure 2: Bar charts of the numbers of different sparticle species observable in a number of benchmark supersymmetric scenarios at different colliders, including the LHC and linear $e^+e^-$ colliders with various centre-of-mass energies. The benchmark scenarios are ordered by their consistency with the most recent BNL measurement of $g_\mu - 2$ and are compatible with the WMAP data on cold dark matter density. We see that there are some scenarios where the LHC discovers only the lightest neutral supersymmetric Higgs boson. Lower-energy linear $e^+e^-$ colliders largely complement the LHC by discovering or measuring better the lighter electroweakly-interacting sparticles. Detailed measurements of the squarks would, in many cases, be possible only at CLIC.

the Universe, which may well consist of massive, weakly-interacting particles, *in which case* they should weigh $\lesssim 1$ TeV.

We expect that the clean experimental conditions at a linear $e^+e^-$ collider will enable many detailed measurements of this new dynamics to be made. If there is a light Higgs boson, its properties will have been studied at the LHC and an $e^+e^-$ collider with CMS energy up to one TeV, but one would wish to verify the mechanism of electroweak symmetry breaking (EWSB) by measuring the Higgs self-coupling associated with its effective potential, which would be done better at a higher-energy $e^+e^-$ collider. Furthermore if the Higgs boson is relatively heavy, measurements of its properties at the LHC or a lower-energy TeV scale $e^+e^-$ collider will quite possibly have been incomplete. As another example, if Nature has chosen supersymmetry, it is quite likely that the LHC and a TeV-scale $e^+e^-$ collider will not have observed the complete sparticle spectrum, as seen in Fig. 2.

Moreover, in many cases detailed measurements at a multi-TeV $e^+e^-$ collider would be needed to complement previous exploratory observations, e.g. of squark masses and mixing, or of heavier charginos and neutralinos. Analogous examples of the possible incompleteness of measurements at the LHC collider can be given in other scenarios for new physics, such as extra dimensions. A Multi-TeV collider will increase the sensitivity range of the LHC by a factor five or more. Even if extra dimensions are discovered before, it would, for example, be fascinating

to study in detail at CLIC a Kaluza–Klein excitation of the $Z$ boson that might have been discovered at the LHC. Other examples of increased physics reach relative to the LHC are

- Z' production: the increase in sensitivity to Z' is about a factor 5 larger at a multi-TeV collider.
- Compositness: the sensitivity to the compositness scale can be increased by a factor 10.
- The sensitivity to triple gauge boson couplings is increased by a factor 10.

Moreover, in case the EWSB is not driven by the Higgs, new phenomena in WW scattering at the TeV scale can be discovered at the LHC but are often difficult to study in detail, while at a multi-TeV collider this region can be probed with very high precision and e.g. new resonances can be measured with high accuracy.

A detailed study of the physics potential of CLIC, including a close integration of experiments at linear $e^+e^-$ colliders with the accelerator, particularly in the final-focus region, has been performed in [6], using preliminary sets of machine parameters. It was demonstrated that, when taking into account a realistic luminosity spectrum and realistic background conditions, precision measurements can be made at a multi-TeV collider. It is important that a high total luminosity is kept since the cross sections of s-channel processes scale as $1/s$ ($s = E_{\text{CMS}}^2$). On the other hand t-channel production rises as $\ln(s)$ and these cross sections get larger than the s-channel ones in the multi-TeV domain. The precise control of the luminosity spectrum will be important for precision measurements. For resonance scans, performed by varying the CMS energy of the machine, narrow, somewhat reduced luminosity spectra yield about the same final precision as the full broader luminosity spectra. But for measurements such as the Higgs self-coupling the total luminosity is most important.

Since CLIC operates in the high beamstrahlungs regime, the background of $e^+e^-$ pairs and hadronic $\gamma\gamma$ interactions is large. This imposes strong requirements on the detector design. With the assumed background numbers based on earlier preliminary parameter sets, the precision is not compromised significantly, but a reduction in background at the interaction point would be certainly beneficial.

The short time between bunches is also a challenge for the detectors. The detectors will not be fast enough to time-stamp individual bunch crossings but one will need to integrate over a bunch train or a large part of it, which means that the backgrounds of several, perhaps as many as 20, bunch crossings will be accumulated. The resulting large number of overlap events is reminiscent of the experimental conditions at the LHC. However the situations here is somewhat different: most of the background activity from $\gamma\gamma$ collisions will be interactions at low CMS energy and therefore will not affect the hard scattering signatures.

In all, the final parameters of CLIC will have a notable influence on the final physics output and particularly on detector design choices, but precision physics will be possible, and the physics/discovery reach will remain large if the total luminosity remains close to $10^{35}$ cm$^{-2}$s$^{-1}$ as it is the case for the new parameter set.


## 3    Main Linac Accelerating Structures

As stated in section 1, the new design of the main beam accelerating structure is a main driver for many of the parameters in this new set.


### 3.1    HDS Design

The HDS design was inspired by the idea that iris slots could be introduced in addition to the damping waveguides in order to improve suppression of long-range transverse wakefields with little increase of the pulsed surface heating. The geometry of the HDS cell is shown in Fig. 3. In fact, the coupling in the HDS of the (dominant) lowest dipole mode to the slots is significantly stronger than the coupling to the damping waveguides. The waveguides are retained because there are higher-order transverse modes with the RF phase advance per cell close to 0 and longitudinal higher-order modes ($TM_{0n}$), which are not coupled to the slots. These modes are generally well damped by the waveguides.

Because the lowest dipole mode is coupled mainly to the slots rather than to the waveguides, and the weak dependence of this coupling on the damping waveguide aperture size, the surface of the cell outer wall can be increased compared to the TDS [3]. This reduces pulsed surface heating, due to a lower current density, while simultaneously improving damping. The corresponding surface magnetic field distribution is shown in Fig. 4 a).

The slots however introduce a number of difficulties which have had to be addressed. One of them is that the surface electric field is enhanced in the area where the slots end in the centre of the iris. This field enhancement is eliminated by forming the beam aperture out of four circular arcs which have a radius larger than the distance $a$ from the beam axis to the iris tip, see Fig. 3. Because the ends of the slots are further from the centre of the cell than the middle of the iris arcs, they are exposed to lower surface electric field, which is shown in Fig. 4 b).

Each cell consequently consists of four quadrants which have no contact because the slots cut both the iris and the wall between damping waveguides of adjacent cells. A structure can thus be formed from four quadrants in which the cells, irises, slots, damping waveguides and other subsystems are milled into the outside of each piece as is shown in Fig. 5.
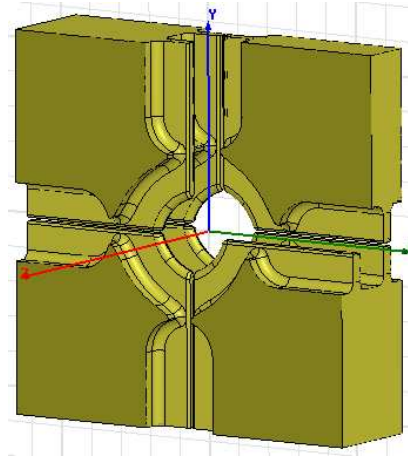
4

Figure 3: Geometry of the HDS cell. Two cells are shown to better demonstrate shape of the cell cavity, slotted iris and damping waveguides. For the same reason one quarter of one of the cells is removed from the picture.
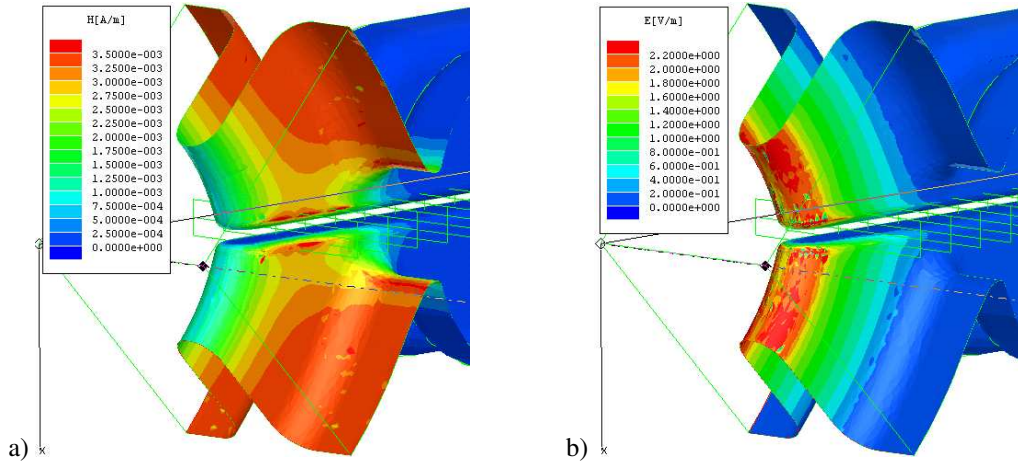


Figure 4: Surface magnetic (a) and electric (b) field distribution in HDS cell.

This novel accelerating structure design and assembly gives a number of advantages compared to traditional structures in which individual cells are brazed together, including

- reduction of the number of pieces per structure to four and a significant decrease in surface area to be machined.
- free choice of joining because there are no RF currents between quadrants.
- no water/vacuum joints nor brazed-on cooling channels.
- excellent vacuum pumping.
- slots can be as narrow as needed and profiled – an important feature for 30 GHz.

Fig. 6 shows a picture of a 60-cell HDS prototype which has been successfully manufactured using high-speed 3D-milling with 5-micron precision.

### 3.2 The Optimisation Procedure

The new structure optimisation procedure was motivated by the need to simultaneously vary iris diameter, iris thickness and RF phase advance per cell while considering the effect on short-range transverse wakefield amplitude, long-range transverse wakefield suppression, RF-to-beam efficiency, surface fields and power flow. The simple approach of varying a single parameter at a time was clearly impractical.

The optimisation procedure, which is repeated for different phase advances, consists of three parts for each fixed RF phase advance. In the first part, a set of nine individually optimised cell geometries are calculated for fundamental-mode and lowest-dipole-mode characteristics for three different apertures $a$, and three different iris thicknesses $d$. This gives a two-dimensional parameter space for interpolation.
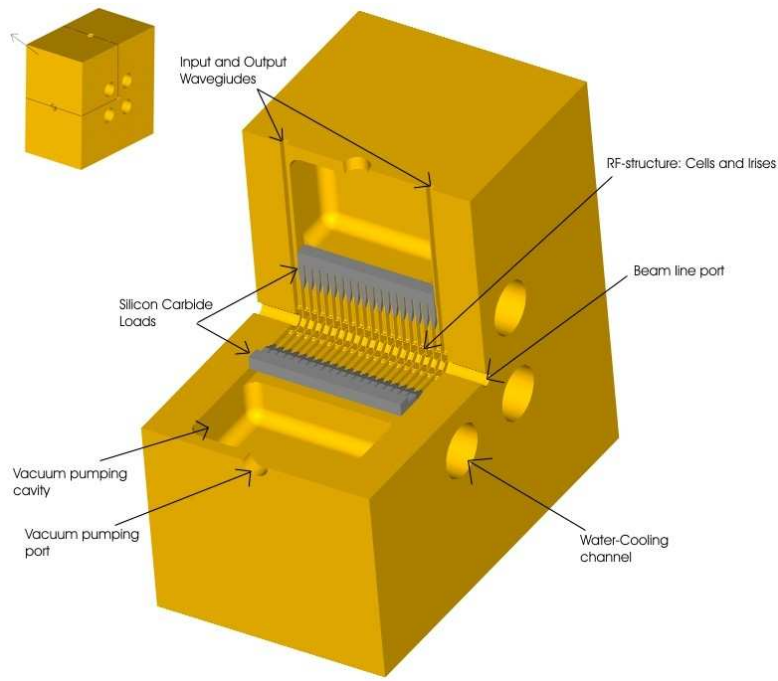
Figure 5: The HDS layout. Taking one of the quadrants out shows the inside of the structure: the accelerating structure cells, the damping waveguides, terminating loads, the vacuum pumping ports, the input and output waveguides, as well as four water-cooling channels.
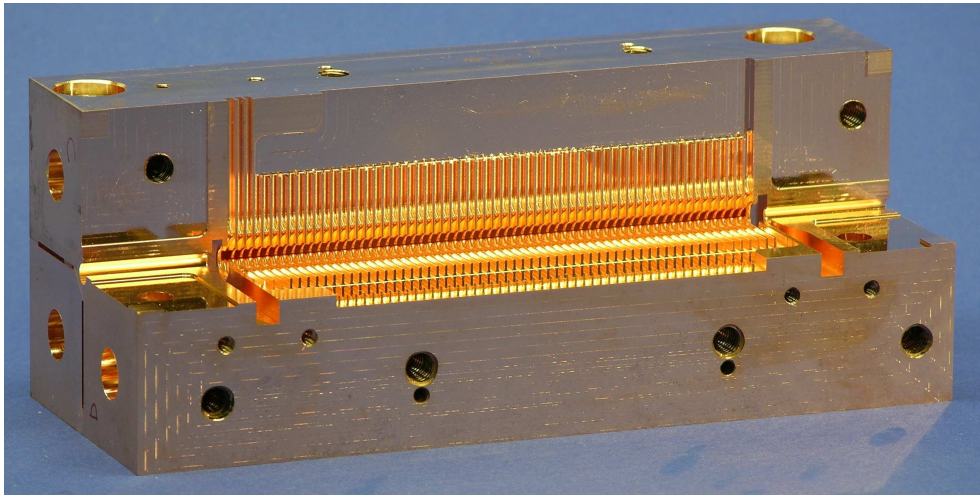


Figure 6: Three quadrants of the HDS 60-cell copper prototype.

In the second part, parameters for $4 \cdot n_{d1} \cdot n_{d2} \cdot (n_{a1}-1) \cdot (n_{a2}-1)/2$ structures are calculated. Here $n_{d1}, n_{d2}, n_{a1}, n_{a2}$ mean number of variation in $d_1$, $d_2$, $a_1$, $a_2$, respectively, which are $d$ and $a$ in the first and last cells of a structure. For each structure the bunch charge $N$ is determined from the results of beam dynamic simulations which take into account the effect of short-range wakefields on emittance growth [2]. The long-range wakefields of the lowest dipole mode are calculated based on interpolated parameters and an uncoupled model. The value of the transverse wake envelope at the position of the second bunch $\|w(N_s\lambda_{\mathrm{RF}})\|$ is limited by the following condition [2]:

$$N \cdot \|w(N_s\lambda_{\mathrm{RF}})\| < 4 \cdot 10^9 \times 10 \text{ kV/pCm}^2 \tag{1}$$

Satisfying this condition gives the bunch separation in the number of RF cycles $N_s$.

In the third part of the optimisation, structures are selected which satisfy the following RF constraints which are based on a structure made from CuZr alloy and Mo iris tips:
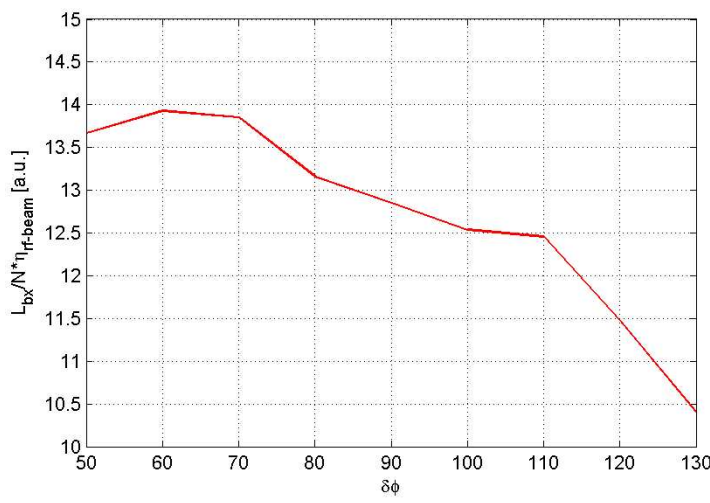
6

Figure 7: Figure of merit versus RF phase advance per cell.

1. Surface electric field [9]: $E_{\mathrm{surf}}^{\max} < 380$ MV/m.
2. Pulsed surface heating [10]: $\Delta T^{\max} < 56$ K.
3. Power [11]: $P_{\mathrm{in}}\sqrt{\tau_p} < 1200$ MW $\sqrt{\mathrm{ns}}$.

Here $E_{\mathrm{surf}}^{\max}$ and $\Delta T^{\max}$ refer to maximum surface electric field and maximum pulsed surface heating temperature rise in the structure, respectively. $P_{\mathrm{in}}$ and $\tau_p$ denote input power and pulse length. Since both $\Delta T^{\max} \propto \sqrt{\tau_p}$ and $P_{\mathrm{in}}\sqrt{\tau_p}$ depend on pulse length conditions, 2 and 3 can always be satisfied by reducing the number of bunches $N_b$ in the train. This reduction is however limited because the shorter the pulse the lower the RF-to-beam efficiency due to the fill time of the structure. Hence, $N_b$ is chosen to make the pulse as long as possible under pulsed surface heating and power constraints. Then, if the structure satisfies condition (1), RF-to-beam efficiency and other pulse length dependent parameters of the structure are scaled for this value of $N_b$.

Though a different choice of optimisation criteria is possible, our main goal is to reach the design luminosity at a given energy in the most efficient way. Hence the optimum structure must provide the highest ratio of luminosity to main linac input power. In terms of the structure parameters this corresponds to maximizing the figure of merit: $L_{b\times}\eta/N$, where $L_{b\times}$ denotes the luminosity per bunch crossing in a 1% energy bin – this is obtained from beam dynamics simulations of the CLIC main linac and beam delivery system [2]. Thus, the optimum structure is that which gives the maximum of figure of merit for all structures satisfying conditions 1 through 3.

It has to be noted that this optimisation procedure is based on a number of assumptions that are the best knowledge as of mid 2005. In the future, these assumptions may well change when new data becomes available. The RF power constraint [11] is the most uncertain number. It is based on X-band data for copper structure, whereas the number we need is for molybdenum structures at 30 GHz. The two other RF constraints, pulsed surface heating and surface electric field, are also not known with any certainty. Finally, since breakdown behaviour is theoretically not well understood, there is no guarantee that there are no other RF constraints.

The optimisation procedure has been performed for a range of RF phase advances $\Delta\phi$ of 50° to 130°. The iris radius $a$ was varied from 1 to 2.5 mm, the thickness $d$ was varied from 0.3 to 0.75 mm for $\Delta\phi < 90°$ and from 0.5 to 1 mm for $\Delta\phi \geq 90°$. A variation step of 0.05 mm was used for both $a$ and $d$, resulting in 217800 analyzed structures for each value of $\Delta\phi$. The results show a maximum figure of merit: $L_{b\times}\eta/N = 14.0$ at $\Delta\phi = 70°$. In this case, the bunch separation is 7 RF cycles. The parameters of the corresponding accelerating structure have been presented in [5]. After discussion it was decided that the number of 7 RF cycles is inconvenient for practical reasons (frequency multiplication) and therefore the number of cycles was increased from 7 to 8. The optimisation has been performed again with this additional constraint. The resulting figure of merit versus RF phase advance per cell is plotted in Fig. 7, which clearly indicates that the best structure has an RF phase advance per cell of 60°.

In Fig. 8, several other parameters of the optimum structure are presented as functions of average iris to wavelength ratio: figure of merit, RF-to-beam efficiency, luminosity per bunch crossing, input power, and bunch population. The maximum of the red line at $<a>/\lambda=0.19$ corresponds to the optimum shown in Fig. 7. The corresponding input power per structure is 190 MW. On the other hand, the figure of merit curve presented in Fig. 8 is rather flat in the vicinity of the optimum. Therefore, a reduction of $<a>/\lambda$ results in very little change of the figure of merit but significantly reduces the input power which is advantageous. A compromise value of 150 MW for the input power has been chosen which is not exactly the maximum of the figure of merit but is very close to it. The reduction of the input power and increase in the RF-to-beam efficiency simplifies the 30 GHz power production
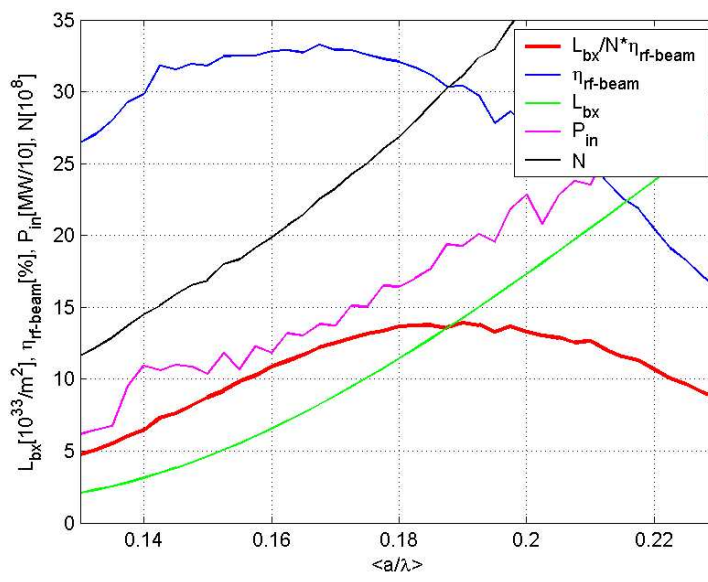
Figure 8: Parameters of the optimum structure as a function of average iris radius to wavelength ratio.

| | |
|---|---|
| $< E_{\mathrm{acc}} >$ [MV/m] | 150 |
| f [GHz] | 29.985 |
| RF phase advance per cell: $\Delta\phi$ [°] | 60 |
| Cell length: $l_c$ [mm] | 1.66635 |
| First and last iris radius: $a_1$, $a_2$ [mm] | 2.06, 1.50 |
| First and last iris thickness: $d_1$, $d_2$ [mm] | 0.275, 0.365 |
| First and last cell Q-factor: $Q_{1,2}$ | 2590, 2244 |
| First and last cell shunt impedance $r_{1,2}$ [(Linac)MΩ/m] | 79, 92 |
| First and last cell group velocity: $v_g/c_{1,2}$ [%] | 12.2, 5.07 |
| Averaged $a$ to wavelength ratio: $<a>/\lambda$ | 0.178 |
| Number of particles in the bunch: $N$ | $2.56 \times 10^9$ |
| Luminosity per bunch crossing: $L_{b\times}$ [m$^{-2}$] | $1.12 \times 10^{34}$ |
| $N_{\mathrm{cell}}$ | 140 |
| Structure length (active): $l$ [mm] | 233 |
| Bunch separation: $N_s$ [RF cycles] | 8 |
| Number of bunches in the train: $N_b$ | 220 |
| Pulse length: $\tau_p$ [ns] | 68.0 |
| Input power: $P_{in}$ [MW] | 151 |
| RF-to-beam efficiency: $\eta$ [%] | 30.9 |

Table 1: Parameters of the best structure calculated without interpolation.

scheme significantly.

A list of the optimised structure parameters, which are finally calculated without interpolation, is presented in Table 1. $\eta$ refers to the RF-to-beam efficiency taking into account the lower electrical conductivity of the Mo tips. Fundamental mode parameters as a function of cell number are shown in Fig. 9 and the transverse wake is shown in Fig. 10.

With the new HDS structure, the overall performance of CLIC in terms of the luminosity to power ratio has been improved while simultaneously satisfying for the first time all the beam dynamics and RF constraints described previously. The main feature leading to the improvement is the reduction in the bunch spacing from 20 to 8 fundamental RF cycles. This has a profound effect on the structure RF-to-beam efficiency which is increased despite the reduction of the pulse length by a factor of two and reduction in bunch charge by 40%.

Though the smaller bunch charge is not advantageous for the luminosity, it has a beneficial effect for the damping rings since the emittance is very strongly influenced by intrabeam scattering (IBS).
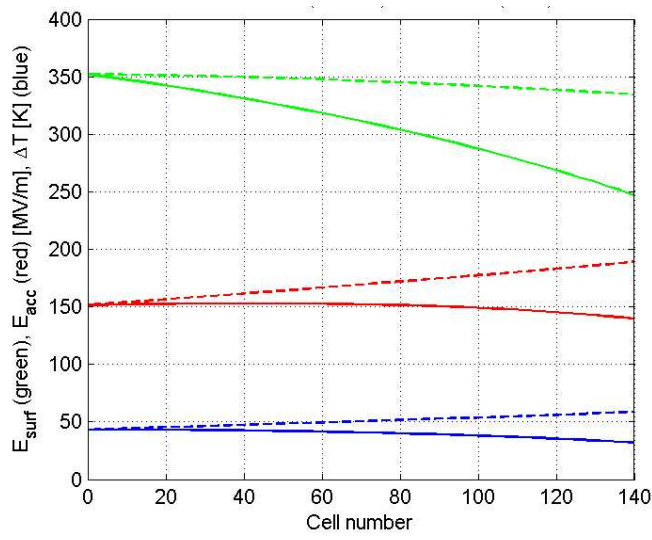
Figure 9: Pulsed surface heating temperature rise (blue), accelerating gradient (red), and maximum surface electric field (green) along the optimum structure with (solid) and without (dashed) beam loading.
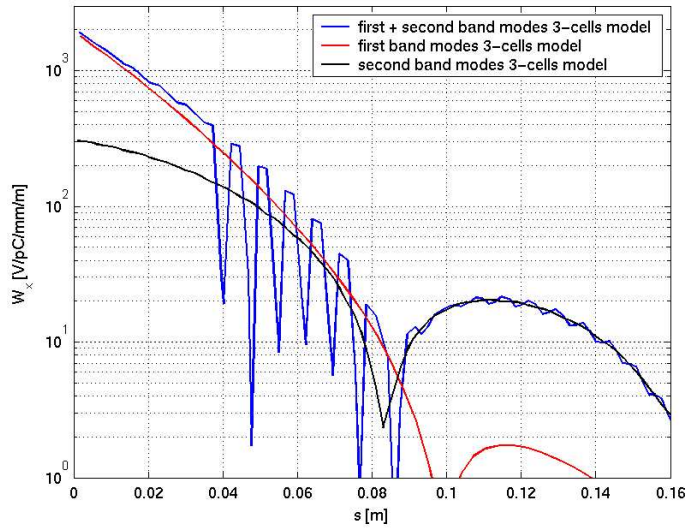


Figure 10: Envelope of the wake of the first (red) and second (black) lowest dipole modes, as well as of the total wake (blue) in the optimum structure.

## 4 Damping Rings

The CLIC damping ring is composed of two long FODO-cell straight sections with wigglers, two TME-cell arcs, and four dispersion suppressors connecting the arcs and the straights, forming a racetrack shape. The beam energy, ring circumference, number of arc cells, length of wiggler sections, wiggler period, wiggler field, and beta function at the wiggler were determined so as to produce beam emittances close to the CLIC target values, taking into account the combined effect of radiation damping, intrabeam scattering and quantum excitation [12, 13]. The emittance growth from intrabeam scattering dominates that from quantum excitation. The optimisation of the ring parameters including the intrabeam-scattering effect distinguishes the CLIC design from other damping rings, like those developed for NLC, TESLA or ILC. For the purpose of parameter optimisation and performance assessment, the emittance growth from intrabeam scattering was computed using the 'modified Piwinski solution' [14, 15].

The ring circumference was made as small as possible, while still maintaining a reasonable ratio of store time over damping time, to keep the RF voltage low and the space-charge tune shift at an acceptable level. The filling factor of dipole and wiggler magnets as a fraction of the whole circumference was maximised, since the radiation damping arises only from the deflecting fields, while intrabeam scattering occurs at all locations around the ring. To maintain a high degree of polarisation for the electrons, the beam energy of 2.424 GeV corresponds to half an integer spin tune, namely $a\gamma = n + 1/2$, with $n = 5$, where $a \approx 1.16 \times 10^{-3}$ denotes the anomalous magnetic

9

| variable | symbol | value |
|---|---|---|
| bunch population | $N$ | $2.56 \times 10^9$ |
| bunch spacing | $T_{\text{sep}}$ | 0.533 ns |
| bunches per train | $N_{\text{b}}$ | 110 |
| number of trains | $N_{\text{train}}$ | 4 |
| store time / train | $t_{\text{store}}$ | 13.3 ms |
| rms bunch length | $\sigma_z$ | 1.547 mm |
| rms momentum spread | $\sigma_\delta$ | 0.126% |
| final hor. emittance | $\gamma\epsilon_x$ | 550 nm |
| hor. emittance w/o IBS | $\gamma\epsilon_{x0}$ | 134 nm |
| final vert. emittance | $\gamma\epsilon_y$ | 3.3 nm |
| coupling | $\kappa$ | 0.6% |
| circumference | $C$ | 360 m |
| beam pipe radius in arc | $b_{\text{arc}}$ | 2 cm |
| vertical half gap in wiggler | $b_w$ | 6 mm |
| no. of arc bends | $n_{\text{bend}}$ | 96 |
| arc-dipole field | $B_{\text{bend}}$ | 0.932 T |
| length of arc bend | $l_{\text{bend}}$ | 0.545 m |
| number of wigglers | $n_{\text{wiggler}}$ | 76 |
| wiggler field | $B_{\text{wiggler}}$ | 1.7 T |
| length of wiggler | $l_{\text{wiggler}}$ | 2.0 m |
| wiggler period | $\lambda_w$ | 10 cm |
| momentum compaction | $\alpha_c$ | $0.796 \times 10^{-4}$ |
| synchrotron tune | $Q_s$ | 0.005 |
| horizontal betatron tune | $Q_x$ | 69.82 |
| vertical betatron tune | $Q_y$ | 34.86 |
| RF frequency | $f_{\text{RF}}$ | 1.875 GHz |
| energy loss / turn | $U_0$ | 2.074 MeV |
| RF voltage | $V_{\text{RF}}$ | 2.39 MV |
| beam energy | $E_b$ | 2.424 GeV |
| damping rime | $\tau_s$ | 1.405 ms |
| revolution time | $T_{\text{rev}}$ | 1.213 $\mu$s |
| repetition rate | $f_{\text{rep}}$ | 150 Hz |

Table 2: CLIC Damping-Ring Parameters

moment of the electron.

For dynamic-aperture reasons, the phase advance over 12 arc cells is $7 \times 2\pi$ in the horizontal plane and $3 \times 2\pi$ in the vertical. These phase advances produce a second order achromat where all second order geometric aberrations cancel (Brown's 1st theorem [16]). The arcs are equipped with nine families of interlaced sextupoles, where each cell accommodates three different sextupoles and the pattern repeats after three cells. To further enhance the dynamic aperture, additional two families of harmonic sextupoles are installed in the two long dispersion-free wiggler sections. After the nonlinear optimisation of the 11 sextupole-family strengths, the normalised dynamic acceptance at injection corresponds to $1600\,\mu$m horizontally and $250\,\mu$m vertically, with a momentum bandwidth of $\pm 1\%$ [17]. In view of the 'flatness' of the dynamic aperture, a pre-damping ring appears to be necessary for both electron and positron beams, unless the electron beam can be produced from a 'flat' electron gun [18]. A further optimisation of the beta-function ratio at the focusing sextupoles and an enhanced dispersion at the sextupoles increase the dynamic aperture, but also the final emittances. Therefore, the present optics can be considered an optimum with respect to the output emittance.

Table 2 summarises the new parameters of the damping ring. The trains are stored for two 150 Hz cycles (13.3 ms), two of them are extracted each cycle and two new ones injected. The bunch charge and bunch spacing are decreased with respect to the 2002 TRC [4], by factors of 1.6 and 2.5, respectively. The wiggler period is reduced by a factor of two, from 20 to 10 cm, since the shorter period is technologically feasible and it reduces the final emittance significantly. The RF voltage and emittance coupling have also been optimised to yield smaller transverse emittances.

Figure 11 illustrates the dependence of the final horizontal and vertical emittances on the bunch population. The four curves refer to two different values of the RF voltage (2.39 MV and 2.59 MV) and to two different emittance coupling values (1.1% and 0.6%). The smallest vertical emittance is achieved for the smaller coupling and lower RF
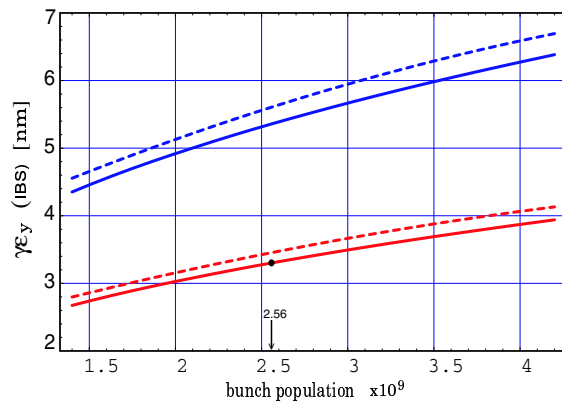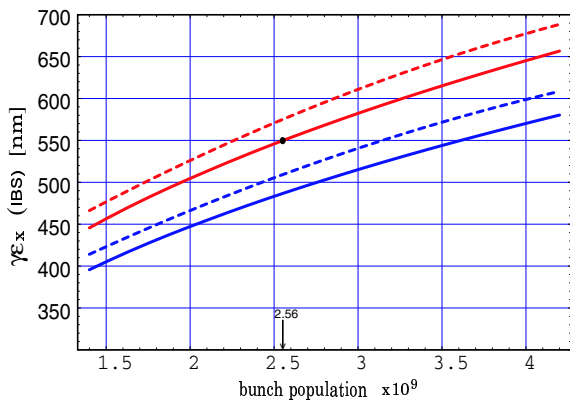
Figure 11: Horizontal (left) and vertical normalised emittance (right) as a function of bunch population. The red curves refer to a coupling of 0.6%, the blue ones to 1.1% emittance coupling. The solid lines are obtained for an RF voltage of 2.39 MV, the dotted ones for 2.59 MV. The wiggler field is 1.7 T and the wiggler period 10 cm.
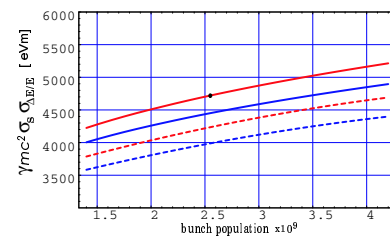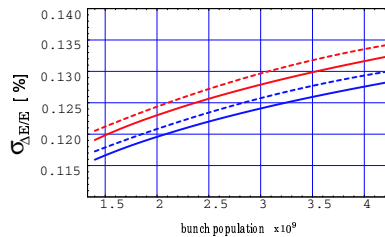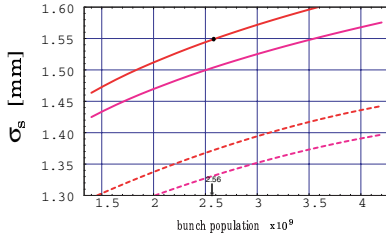


Figure 12: Bunch length (left), energy spread (centre), and longitudinal normalised emittance (right) as a function of bunch population. The red curves refer to a coupling of 0.6%, the blue ones to 1.1% emittance coupling. The solid lines are obtained for an RF voltage of 2.39 MV, the dotted ones for 2.59 MV. The wiggler field is 1.7 T and the wiggler period 10 cm.
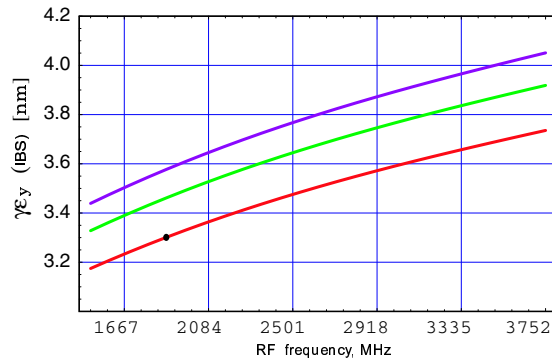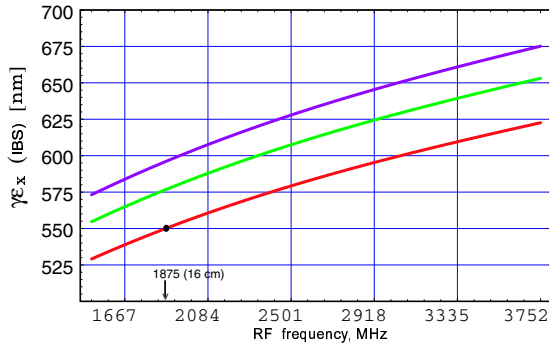


Figure 13: Horizontal (left) and vertical normalised emittance (right) as a function of RF frequency. The three curves refer to RF voltages of 2.79, 2.59 and 2.39 MV, from top to bottom. The wiggler field is 1.7 T and the wiggler period 10 cm. The black spot indicates the nominal RF frequency.

voltage. Figure 12 shows the associated values of rms bunch length, rms energy spread, and longitudinal emittance. The dependence of the transverse emittances on the RF frequency and RF voltage is shown in Fig. 13. Doubling the RF frequency increases both transverse emittances by about 15%. At the same time the longitudinal emittance decreases by about 30% (not shown).

Figures 14 and 15 present the time evolution of the two transverse emittances, and the longitudinal beam sizes, respectively, as computed with and without taking into account the intrabeam scattering. The intrabeam scattering leads to a quadrupling of the two transverse emittances. The total time span shown corresponds to about twice the nominal store time of 13.3 ms. An equilibrium is reached before beam extraction.

Figure 16 shows the time evolution of the transverse emittances for different wiggler fields. Figure 17 gives the
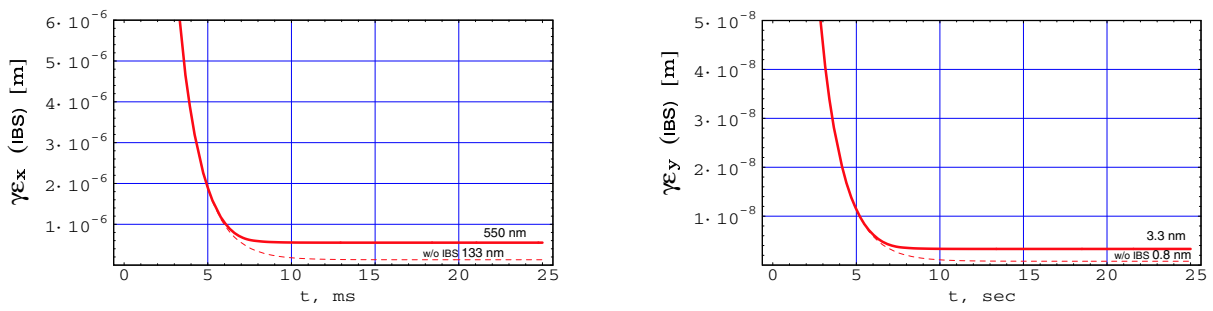
11

Figure 14: Horizontal (left) and vertical normalised emittance (right) as a function of time during the store with (solid) and without intrabeam scattering (dashed). The wiggler field is 1.7 T and the wiggler period 10 cm.
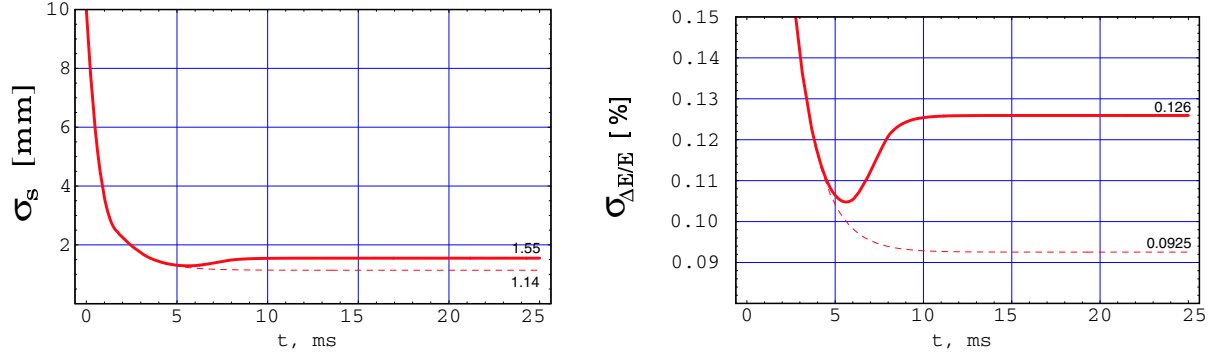


Figure 15: Bunch length (left) and energy spread (right) as a function of time during the store with (solid) and without intrabeam scattering (dashed). The wiggler field is 1.7 T and the wiggler period 10 cm.
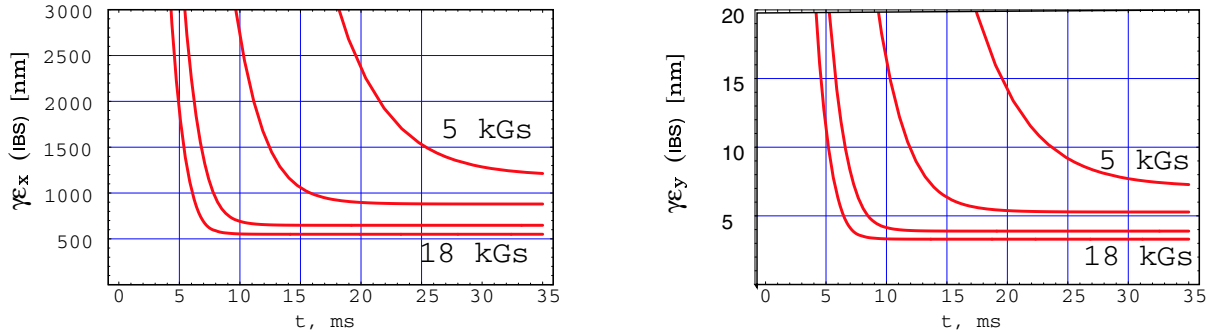


Figure 16: Horizontal (left) and vertical normalised emittance (right) as a function of time during the store with intrabeam scattering for wiggler fields of 0.5, 1.0, 1.5 and 1.8 T (from top to bottom), and a wiggler period of 10 cm.

dependence of the final transverse emittance on the wiggler field and the wiggler period. The reduction of the wiggler period from 20 cm to 10 cm reduces the two transverse emittances by about 30%. The further decrease to 8.5 cm offers no significant additional gain.

A noteworthy feature of the revised design parameters is that two trains are extracted simultaneously and need to be combined using a subsequent delay line and RF deflectors. The advantage is a two times larger bunch spacing in the ring (16 RF cycles at 30 GHz) compared with the main linac (8 RF cycles), which alleviates the impact of electron-cloud and fast-ion instabilities, and allows for a lower (but still higher than usual) RF frequency in the ring, which also leads to a longer bunch and reduces the intrabeam scattering.

The parameters in Table 2 do not include any margins or overheads for errors and tolerances, nor for any collective effects other than intrabeam scattering.

The primary contributions to the vertical emittance are spurious vertical dispersion and betatron coupling. The effects of misalignments was simulated by the BETA code and by a MAD-based dispersion-free steering routine
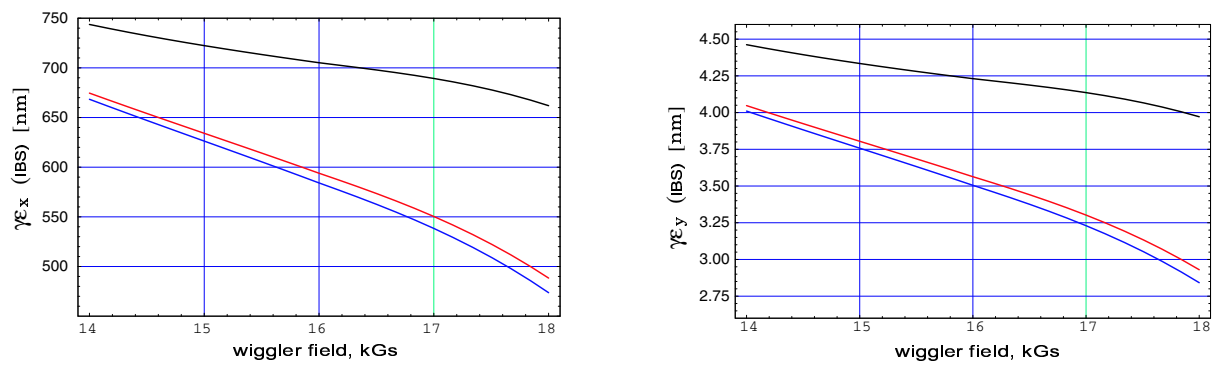
Figure 17: Horizontal (left) and vertical normalised emittance (right) as a function of the wiggler field for a wiggler period of 20, 10 and 8.5 cm (from top to bottom).

| | |
|---|---|
| Energy | 2.424 GeV |
| Bunch charge (# of particles) | $3.4 \times 10^9$ |
| Horizontal emittance (norm. r.m.s.) | $\leq 44\mu$m |
| Vertical emittance (norm. r.m.s.) | $\leq 7\mu$m |
| Energy spread | $\leq \pm 0.5\%$ |
| Bunch-length (r.m.s.) | $\leq 5$ mm |
| Number of bunches per train | 110 |
| Bunch spacing | 16 cm |
| Number of trains per pulse | 2 |
| Spacing between trains | 72.64 m |
| Rep. rate | 150 Hz |
| vertical polarisation of electrons | $\geq 80\%$ |

Table 3: Main beam injector specification for electron beam. The reference point is the damping ring injection. The same specifications are valid for positrons except for the polarisation, which is only considered as an upgrade option.

previously used for LEP operation [19]. Considering rms displacements of 100 microns for quadrupoles and 30 microns for sextupoles, a combined closed-orbit and dispersion correction reduces the rms orbit distortion to less than 50 microns and the rms vertical dispersion to 4 mm. The vertical emittance for these conditions is still larger than 20 nm [19]. The design emittance would correspond to an rms orbit offset at the sextupoles of less than 10 microns [19]. To reduce the vertical emittance in the presence of errors towards the target value of 3.3 nm, a number of options are available, such as an optimisation of the BPM locations as well as an increase in the number of BPMs or correctors, the beam-based alignment of BPMs with respect to adjacent quadrupoles, and a correction of both residual vertical dispersion and betatron coupling by means of a large number of distributed skew quadrupoles, as is employed at the KEK/ATF. The errors will not only increase the equilibrium emittance, but also reduce the dynamic aperture.

Limitations from collective effects are studied in [20]. The results suggest that countermeasures must still be developed for the electron cloud in the positron damping ring [21] and for the fast beam-ion instability in the electron ring. The space charge tune shift is somewhat marginal in either ring, but probably acceptable. No serious constraints are expected to arise from longitudinal microwave instability, TMC instability, coherent synchrotron radiation, Touschek effect, and resistive-wall coupled-bunch instabilities.

## 5    Injector Specifications

The injector requirements are to a large extent determined by the damping ring parameters in the previous section. These requirements are summarised in Table 3. The reference points for the specification are the injection beam lines of the main electron and positron damping rings.

The bunch charge specification contains a margin for a maximum of 20% injection losses. The specifications for the transverse emittances are obtained by dividing the dynamic acceptance of the damping ring (without orbit and alignment errors) by a factor 36, corresponding to a $6\sigma$ acceptance aperture. Probably pre-damping rings will be required to achieve these emittance requirements. Pre-damping rings for this purpose have already been considered in [13]. The longitudinal beam parameters are in line with the assumptions for the injected beam from section 4

13

with a safety factor 2 for both bunch length and energy spread. The required longitudinal parameters are not particularly challenging.

For the spacing in between the trains we assume that the damping rings operate with 4 stored trains equidistantly distributed around the ring circumference. On every machine pulse two subsequent trains are extracted and immediately replaced by two trains from the injector.

The CLIC injector scheme for the old parameter-set has been published in [23, 24, 25]. An adaptation of this injector scheme to the new parameters still needs to be performed. Since the total number of positrons needed per pulse is slightly reduced in comparison with the old parameters no major feasibility limitations are expected. The new bunch spacing of 16 cm, however, requires a change of RF frequencies throughout the injector complex. Another additional complication comes from the need to provide two trains of bunches with 73 m spacing in each injector pulse.

## 6    Beam Dynamics from Damping Ring to BDS

After the damping ring, the beam is accelerated to 9 GeV and longitudinally compressed in a two-stage bunch compressor. The design of these compressors will be studied in the framework of EUROTeV [26]. Previous studies indicated that they are feasible [27].

Two damping ring beam pulses will be merged to form one main linac pulse. This will reduce the bunch distance from 16 cm to 8 cm. Different options exist how this can be done, e.g. using RF deflectors. The exact scheme will need to be determined by performing a full optimisation of the compressor complex including the acceleration between the two stages, which could use high (15 GHz) or low frequency (e.g. 1.875 GHz).

Due to the high RF frequency the longitudinal and transverse wakefields in the CLIC main linac are quite strong. The main linac lattice has therefore to be designed with special attention to the minimisation of the effects caused by these wakes. The lattice for the previous parameter set has been derived in a careful optimisation of the focusing strength along the linac, see reference [28].

The lattice is based on a sequence of FODO cells, with a constant phase advance per cell and a cell length that scales with $\sqrt{E}$. Simulations with these scalings showed excellent performance. In addition, this combination keeps the fill factor along the linac constant which helps to keep constant the length of each main linac section that is powered by one drive beam decelerator. The real lattice was a discrete approximation of the scaled lattice which consisted of 13 sectors of FODO cells; in each sector the cell length was constant. This was due to the fact that the old linac lattice consisted of five different girder types that all had the same length of 2.23 m (including the bellows which connect adjacent girders). The main accelerating girder supported four structures. Then four different girder types existed, where the first one, two, three, or all accelerating structures were replaced with a quadrupole. The new lattice will be quite similar to the old one except that the girder length is only 2.06 m (see section 8). The emittance preservation properties of the new and old lattice can thus be expected to be comparable, but a full study remains to be done once the new lattice has been designed.

In the linac, the beam is accelerated off the crest of the RF wave. This is necessary since the single bunch longitudinal wakefields introduce an energy spread in the beam. The fields induced by the beam head is decelerating the beam tail. If the beam arrives slightly before the crest of the accelerating RF, the tail will be accelerated more than the head. This can be used to counterbalance the wakefield induced effect. For the old parameters it was required that the beam has an energy spread of less than 1% full width at the end of the linac and that the beam is accelerated by not more than $15°$ off-crest. These constraints have been used to determine for each structure the minimum bunch length as a function of the bunch charge. For the new parameters exactly the same procedure was used.

The transverse wakefields of the structure are the main source of emittance growth. This growth depends on the lattice design. Since the old design had been optimised thoroughly to minimise the wakefield effects, it was assumed that no better solution can be found for the new lattice, if one does not want to decrease the fill factor. Consequently the constraint was set that the new beam should see the same transverse wakefield effects as the old one. As a simple measure for this, the amplitude of the wake kick over a bunch length was used. It was required that $N \cdot w(2\sigma_z)$ be the same for the old and new parameters. Consequently the transverse effects are expected to be the same for the new and old parameters.

In addition to the single bunch wakefields, another concern are the multi-bunch transverse wakefields, which can lead to multi-bunch beam break-up. Simulations have shown that the additional effects from the multi-bunch wakefields can be neglected in comparison to the single bunch effects for a transverse wakefield amplitude of $20 \, \text{kV/pCm}^2$ and a bunch charge of $4 \times 10^9$. For a given structure design, the multi-bunch wakefields can be reduced by spacing the bunches further apart. In the optimisation a constraint $w(N_s \lambda_{RF}) \cdot N / 4 \times 10^9 \leq 10 \, \text{kV/pCm}^2$ (see Eq. 1) has been respected. The multi-bunch effects should therefore be acceptable as a first simulation of the multi-bunch beam break-up indicates. Figure 18 shows the ratio of the multi bunch to the single bunch emittance growth for an initial offset.
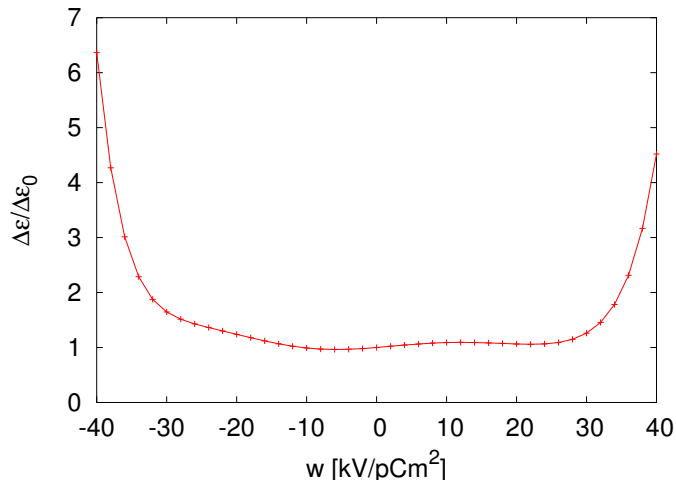
14

Figure 18: The emittance growth $\Delta\varepsilon$ for a bunch train with an initial offset. The value $\Delta\varepsilon$ for a full train is compared to that for a single bunch $\Delta\varepsilon_0$ as a function of the wakefield amplitude at the second bunch. The bunch charge is $2.56 \times 10^9$ particles.

## 7    Beam Delivery, Collimation and Backgrounds

The CLIC 3 TeV beam delivery system (BDS) downstream of the main linac consists of a 2 km long collimation system, which is followed by a 0.5 km long final focus. The total length of the BDS, counting both sides of the interaction point, is 5 km. The collimation system itself consists of two parts, the first longer part devoted to energy collimation, the second shorter part to betatron collimation. A detailed description of the CLIC BDS can be found in Ref. [29] and additional information on the collimation system in [30].

The collimation system was derived from a 1 TeV NLC design generated by Tenenbaum [31]. To render synchrotron-radiation effects at 3 TeV acceptable, all lengths in the energy collimation section were increased by a factor 5, and the bending angles reduced by a factor 12/5 compared with the NLC design. To keep the system short, half of the original energy-collimation system was omitted. The dispersion at the location of the energy spoiler is maintained just large enough to ensure the survival of the energy spoiler, if it is hit by a beam, provided the spoiler is made from carbon, diamond, or possibly beryllium.

The reason to place energy collimation in front of betatron collimation, and to demand a minimum spot size at the energy spoiler is the following. A failure mode analysis for CLIC revealed that off-energy beams with close to nominal emittance are a likely event, against which the downstream system should be protected, and in particular that a rigorous and safe collimation in energy will intercept beams that otherwise would hit the subsequent betatron collimators for most of the failures considered [32]. Rare failures leading to pure betatron oscillations, e.g, misfiring of a damping-ring extraction kicker, are exceptions. These are not only less probable but, in addition, almost always accompanied by a significant emittance blow up in the linac.

The optics of the final focus was derived from the compact NLC 1 TeV final-focus optics of Raimondi and Seryi [33]. The sextupole strengths were increased by a factor 3.4, profiting from the smaller geometric emittance, and the bending angles decreased accordingly, thereby reducing the effect of synchrotron radiation. The exact value of the scale factor was chosen to maximise the luminosity for the nominal emittance. The compact optics was adopted instead of the more conventional even-dispersion optics ($D^* = D'^* = 0$) previously created [34], because it provides for a larger free length $l^*$ from the last quadrupole to the IP, a wider momentum bandwidth, and reduced beam tails [35]. A disadvantage of the compact optics is the tighter collimator setting requirement in the horizontal plane, due to the increased $l^*$ and the dispersion across the final doublet.

Table 4 lists selected parameters of the CLIC BDS. The IP beta functions can be varied easily using a set of five quadrupoles at the entrance of the final focus. The IP beta functions listed yield the largest geometric luminosity, without pinch and without hourglass effect. These values are also close to those yielding optimum luminosity, when beam-beam effects are included [2].

The bunch density at the interaction point is so high that the colliding beams focus each other strongly. Even the transverse beam size is significantly decreasing during the collision. This process increases the luminosity but due to the bending of the particle trajectories it also leads to the emission of beamstrahlung. The average energy of the emitted photons is very high – of the order of 10% of the particle energy – and also the probability of emission is high – of the order of one photon per beam particle. The fact that particles collide after emission of beamstrahlung leads to the development of a luminosity spectrum. For the physics mainly the part of the luminosity close to the

| parameter | Symbol | value |
|---|---|---|
| FF length | | 0.5 km |
| CS length | | 2.0 km |
| BDS length | | 2.5 km |
| bunch population | $N$ | $2.56 \times 10^9$ |
| number of bunches / train | $N_b$ | 220 |
| horizontal emittance | $\gamma\epsilon_x$ | 0.68 $\mu$m |
| vertical emittance | $\gamma\epsilon_y$ | 0.01 $\mu$m |
| horizontal IP beta function | $\beta_x^*$ | 7 mm |
| vertical IP beta function | $\beta_y^*$ | 90 $\mu$m |
| horizontal IP core spot size | $\sigma_x^*$ | 60 nm |
| vertical IP core spot size | $\sigma_y^*$ | 0.7 nm |
| ideal horizontal IP spot size | $\sigma_{x0}^*$ | 37 nm |
| ideal vertical IP spot size | $\sigma_{y0}^*$ | 0.5 nm |
| bunch length | $\sigma_z$ | 30.8 $\mu$m |
| IP free length | $l^*$ | 4.3 m |
| crossing angle | $\theta_c$ | 20 mrad |
| repetition rate | $f_{\rm rep}$ | 150 Hz |
| luminosity without pinch | $L_0$ | $3.6 \times 10^{34}$ cm$^{-2}$s$^{-1}$ |
| ideal luminosity without pinch | $L_{00}$ | $9.3 \times 10^{34}$ cm$^{-2}$s$^{-1}$ |

Table 4: Beam-Delivery System Parameters

nominal centre-of-mass energy is relevant. Hence some part of the luminosity will not be useful any more. For otherwise fixed beam parameters the luminosity is proportional to $1/(\sigma_x\sigma_y)$ while the beamstrahlung increases as $1/(\sigma_x + \sigma_y)$. In all linear colliders one therefore uses flat beams with $\sigma_x \ll \sigma_y$, which minimises the product but maximises the sum of the two beam dimensions. One therefore aims to minimise $\sigma_y$ which will lead to more luminosity in all cases. The choice of $\sigma_x$ however is a trade-off between more luminosity (smaller $\sigma_x$) and a better luminosity spectrum (larger $\sigma_x$).

Due to the nonlinear and chromatic aberrations of the final focus for the strongly squeezed optics the IP beam size is highly non-Gaussian even when not taking into account the beam-beam effect. 15.2% of the population lie outside of $3\sigma_y$ in the vertical plane, and about 7% in the horizontal plane [36]. The rms spot sizes widely overestimate the size of the beam core. The horizontal rms size is of order 100 nm, compared with a core size from a Gaussian fit of 55 nm. In the vertical plane, the discrepancy is larger still, with about 3.5 nm for the rms value and 0.7 nm for the core size. The beam sizes obtained from different tracking codes (MAD, DIMAD, Merlin and PLACET) differ by about 25%.

The emittances in Table 4 refer to the input emittances at the start of the collimation system. The value of 0.68 $\mu$m for the horizontal emittance was recently reduced to 0.66 $\mu$m [37]. However, all calculations and numbers in this section still refer to the 0.68 $\mu$m value.

The geometric luminosity (without pinch effect) obtained by particle tracking is $3.6 \times 10^{34}$ cm$^{-2}$s$^{-1}$ which falls substantially short of the ideal value $9.3 \times 10^{34}$ cm$^{-2}$s$^{-1}$ computed from the ideal linear spot size. Without the collimation system, the luminosity in the tracking is $4.8 \times 10^{34}$ cm$^{-2}$s$^{-1}$ which is 25% larger than that for the full system and two times smaller than the target value. The loss in luminosity is due, in roughly equal parts, to the effect of synchrotron radiation and to higher-order chromo-geometric aberrations.

The finite bandwidth of the beam delivery system also introduces a tight tolerance for the RF gradient and RF phase in the linac. Without the collimation system the tolerance is relaxed by about 70% [38].

With the present emittances and beam delivery system design one however finds that the horizontal spot size cannot be reduced to a level beyond about 60 nm. Using the realistic energy spread and emittances from the main linac, tracking through the beam delivery system and using full simulation of the beam-beam effects one finds the luminosity to be $6.5 \times 10^{34}$cm$^{-2}$s$^{-1}$ and the luminosity above 99% of the nominal centre-of-mass energy to be about $3.3 \times 10^{34}$cm$^{-2}$s$^{-1}$.

Ultimate limits to the IP horizontal spot size are the beamstrahlung, requiring [2]

$$\sigma_x \geq 22.5 \text{ nm } \frac{N}{4 \times 10^9} \sqrt{\frac{\sigma_z}{20 \ \mu\text{m}}} \approx 18 \text{ nm } , \tag{2}$$

and the horizontal Oide effect yielding [39] $\sigma_x \geq 30$ nm. Fundamental limits to the vertical spot size are the quantum diffraction [40] ($\gamma\epsilon_y \geq \lambda_e/2 \approx 0.2$ pm $\rightarrow \sigma_y^* > 5$ pm), the hourglass effect ($\sigma_y \geq 0.4$ nm), and the
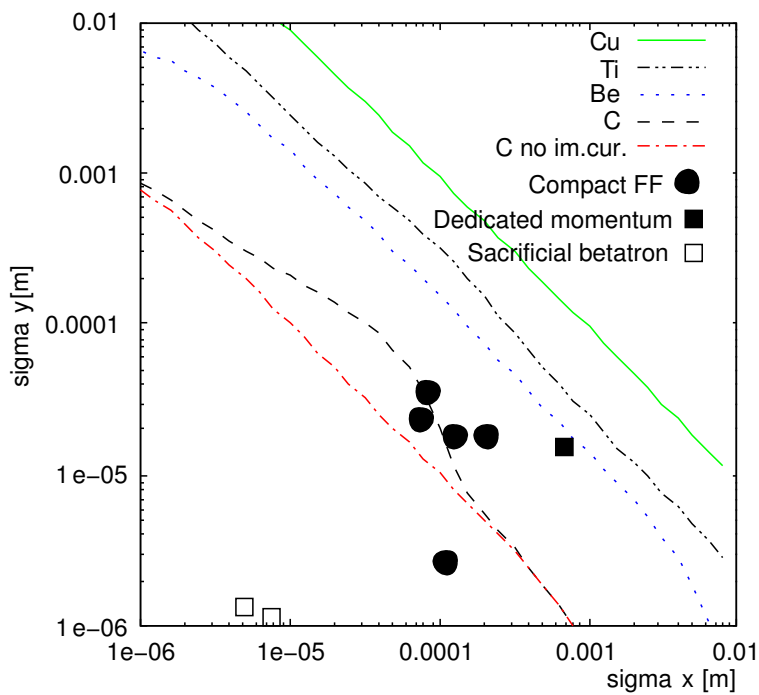
16

Figure 19: Vertical vs. horizontal beam size required for spoiler survival with different spoiler materials [42] and beam-size values at spoiler locations computed from the design beta functions, emittances and energy spread.

vertical Oide effect [39] ($\sigma_y \geq 1$ nm). The above estimate of the vertical Oide effect is pessimistic on the one hand since it considers the rms beam size, on the other hand it is optimistic, since the effect from the horizontal position in the final quadrupole is not taken into account.

The background level at the IP for the present parameters is given in Table 13. Per bunch crossing it is reduced compared to the old parameters, per unit time it remains about the same. The number of beamstrahlung photons per electron is down from 1.5 to 1.1 and the coherent pair production is significantly reduced.

The luminosity performance of the CLIC BDS at 3 TeV is comparable to the performance of the latest NLC system when operated at 3 TeV with CLIC beam parameters [41]. A difference is the length of the two systems. The NLC optics has a length of 1.7 km, the CLIC one is slightly longer than 2.5 km. The maximum dispersion in the NLC system is about 0.2 m, compared with 0.5 m for CLIC. The large dispersion was chosen intentionally for CLIC in order to guarantee the energy-collimator survival in case of beam impact [42]. If we opt for carbon as collimator material and give up the possibility of using beryllium, we might reduce the horizontal beam size at the spoiler by a factor of about 3, as illustrated in Fig. 19. This may allow a significant reduction of the energy collimation, making the length comparable to that of the NLC optics.

The parameters in Table 4 do not include any margins or overheads for errors and tolerances, nor for any collective effects, like wake fields. From the vibration and active stabilisation measurements performed by Redaelli at CERN, a luminosity loss of 25–30% due to fast ground motion is expected [43]. In addition, a 20% luminosity loss was estimated for the 1996 NLC design due to limited beam-based tuning precision for 16 important aberrations [44]. If we do not improve the tuning and stabilisation procedures beyond those assumed in [43, 44] for the CLIC BDS, we could expect a total luminosity loss of up to 50% due to errors.

## 8    Linac Module Layout and PETS (Power Extraction Transfer Structure)

### 8.1    Module Layout

The CLIC two-beam configuration along most of the length of the main and drive linacs (excluding special diagnostic sections for example) consists of repeated 'modules'. Each module contains a PETS (see section 8.2), feeding four accelerating structures, and a drive-beam quadrupole, as a very dense lattice is required for the low-energy drive beam. Two modules are mounted on each alignment girder, and a schematic view of this layout is shown in Fig. 20. Space for quadrupoles in the main linac is made by leaving out one, two or four accelerating structures and replacing the PETS with shortened lower-power versions. The stagger between the two linacs is made to give the correct relative RF to beam timing.

The module length is determined mainly by the length of an accelerating structure and the fact that a PETS feeds four structures (a number which depends on the high-power capability of the PETS which will be determined
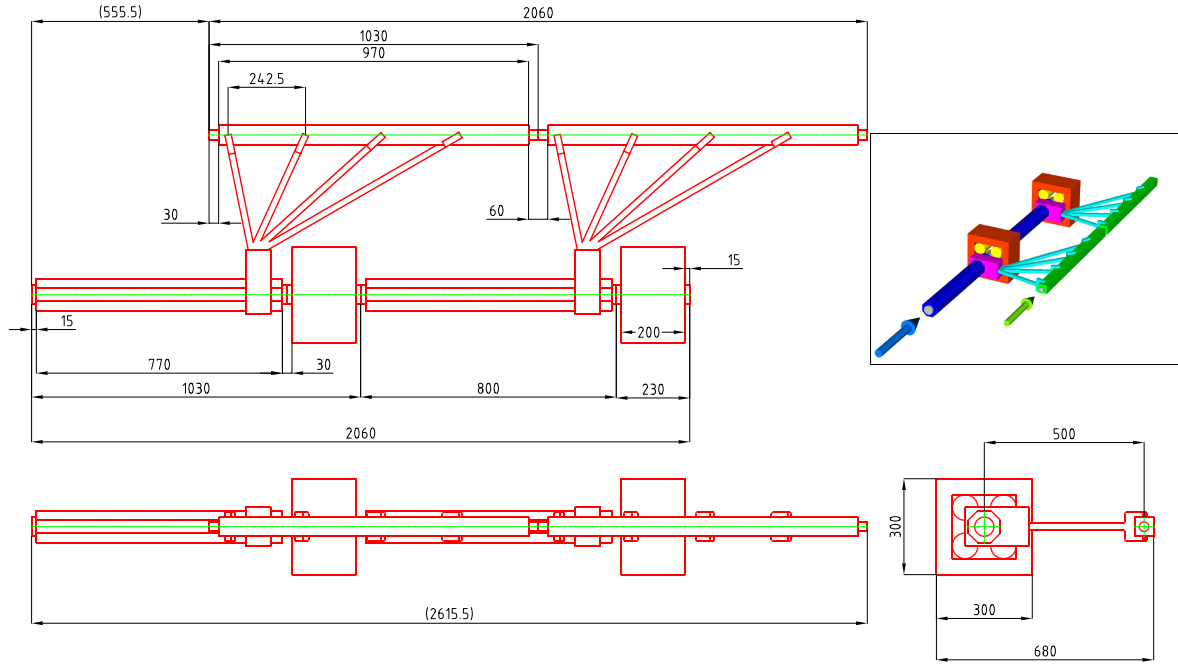
17

Figure 20: Schematic view of the module layout.

in the CTF3 30 GHz experimental program). Drive linac beam dynamics simulations show that the drive beam quadrupole spacing must be about 1 m with a quadrupole length of about 200 mm for sufficient strength. The remaining space, 770 mm, is then available for the PETS which is just sufficient. A 30 mm length has been reserved for component interconnection, however no detailed mechanical design has yet been made.

The regions where each drive beam is fed into and out of a drive beam linac sector have not been designed in detail.

## 8.2    CLIC Power Extraction and Transfer Structure (PETS)

The CLIC Power Extraction and Transfer Structure (PETS) is a passive microwave device in which bunches of the drive beam interact with the impedance of the periodically corrugated waveguide and excite preferentially the synchronous $TM_{01}$ mode at 30 GHz. In the process the beam kinetic energy is converted into electromagnetic energy at the mode frequency, which travels along the structure with the mode group velocity [45]. The RF power produced is collected at the downstream end of the structure by means of the Power Extractor and conveyed to the main linac structure by means of rectangular waveguides.

The choice of PETS geometry is a result of multiple compromises between drive beam stability along the whole decelerator sector ($\sim$600 m) and the active length of the PETS given by the main linac RF power needs and the layout. Surface electric field, power extraction method, HOM damping, ability to cancel RF power generation if needed, and fabrication technology were all evaluated to ensure a reliable design. The final PETS design consists of a 22.5 mm diameter circular waveguide with shallow ($\sim$1.3 mm deep) sinus-type corrugations with 140 degrees phase advance per period (3.8885 mm). Eight HOM damping slots are placed symmetrically around the circumference splitting the whole structure into 8 identical pieces. To simplify the fabrication, the active profile of each of the 8 racks was chosen to be flat, see fig. 21. The damping slot width (2 mm) and the slot's rounding radii (0.8 mm) provide a quasi-constant surface electric field distribution with a maximum of about 110 MV/m at the nominal RF power level. In this configuration the 600 mm PETS active length is sufficient to extract 642 MW of RF power from the 181 A, 15 GHz drive beam. Assuming an extraction and transfer efficiency of 94% this is enough to deliver the required 151 MW to each of the four accelerating structures (see section 3). The CLIC PETS parameters are shown in Table 5.

18

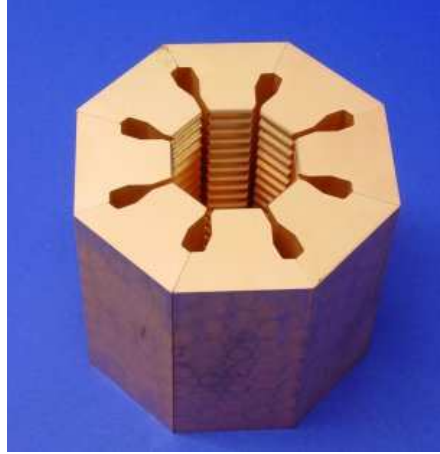| | |
|---|---|
| Synchronous frequency | 29.9855 GHz |
| Aperture | 22.5 mm |
| R/Q | 320.2 $\Omega$/m |
| Group velocity | 0.798 $c$ |
| Phase advance/cell | 140º |
| Active length | 0.6 m |
| Drive beam Current | 181 A |
| RF power generated | 642 MW |
| Extraction and transfer efficiency | 94% |
| Damping slots | 8 x 2 mm |

Table 5: The CLIC PETS parameters



Figure 21: The PETS machining test prototype

### 8.3 PETS Power Extractor

The extraction of RF power from over-moded waveguides is not a trivial task. To make it efficient and compact a new broad-band 8-channel quasi-optical extraction coupler based on the multimode mixing approach has been designed to couple out the power from the CLIC PETS with an efficiency of 98% [46]. The latest version of the coupler consists of two parts, a mode launcher, and a diffraction/extraction section; these units provide an efficient step-by-step conversion of the energy from the $E_{01}$ mode of the over-moded circular waveguide to the fundamental $H_{10}$ mode of the eight radial standard rectangular waveguides. The total length of the extractor is 70 mm. A low power prototype (see fig. 22) has been built and RF tested and shown to be in good (within 1%) agreement with HFSS simulations. Since the PETS is very over-moded, any geometrical perturbation will provoke coupling of the decelerating mode into unwanted HOMs. As a result, a long adiabatic matching section with a number of gradually reduced corrugations between the active PETS part and the power extractor is needed. The matching section has a total length of 58 mm (15 periods) and has a reflection and mode conversion expected to be less than $-40$ dB. Finally the total mechanical length of the PETS including all elements is 770 mm.

### 8.4 PETS HOM Damping

To avoid drive beam losses along the decelerator, the strong suppression of the transverse HOM is absolutely necessary. The most dangerous transverse mode has a frequency and group velocity practically identical to the decelerating one. The only way to damp it is to use its symmetry properties. The damping mechanism of this mode can be explained as a coherent radiation of many RF sources represented by the individual period of the corrugations into eight infinite radial slots.

The angle of radiation here depends on the phase advance and the distance between periods. The higher the phase advance, the smaller the angle and the less the damping. In any case the radiation (damping) is the strongest when the phase advance and period are matched in frequency. In the actual design, the infinite slot is replaced by a broad-band RF matched load. The iterative optimisation of the slot configuration and the damping was done using HFSS [47], GdfidL [48] was used to verify the whole structure behaviour in time domain. Finally beam dynamic simulations with PLACET [49] were used to confirm stable beam transportation along the decelerator.

It was found, that in the presence of the damping slots, the lowest transverse mode splits into two different

Figure 22: Low RF power prototype of the PETS Power extractor

|  | mode 1 | mode 2 |
| --- | --- | --- |
| $W_t$ [V/pC/m/mm] | 2.144 | 0.874 |
| f [GHz] | 28.031 | 35.092 |
| Group velocity [$c$] | 0.8883 | 0.6512 |
| Q loaded | 44.1 | 39.8 |

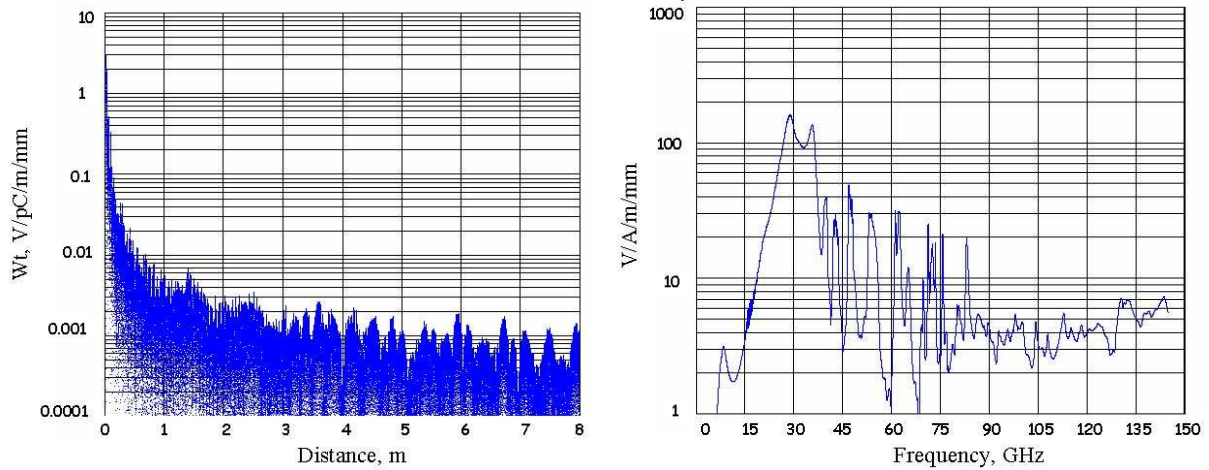Table 6: The lowest transverse modes in PETS



Figure 23: The PETS transverse wake envelope and impedance

frequency modes with different phase relations between slots and aperture. This brings extra benefits due to the naturally introduced quasi-detuning and hence stronger suppression of the wake at shorter distances. In addition the depth of the regular part of the slots was tuned in pairs of 4 to provide the best damping of each of two modes. The parameters of these modes calculated using HFSS are shown in Table 6.

Beam dynamic simulations have shown that insufficiently damped HOM of the higher bands can be troublesome, even though their impedances are quite small [50]. To avoid this, frequency detuning was introduced using a linear increase of the phase advance per cell (from 132 to 140 degrees) along the structure, while keeping the aperture constant. This resulted in an effective suppression of the higher bands HOM by a factor of ten. The final envelopes of the transverse wake and impedance as simulated with GdfidL for the full structure length and single bunch rms size of 0.7 mm are shown in Fig. 23.

The envelopes of a $3\sigma$ beam with an initial offset of $\Delta y = 0.3\,\sigma_y$ along the decelerator with and without transverse wakes simulated with PLACET are shown in Fig. 24. One can see that the transverse HOM have now practically no effect on the beam transport.
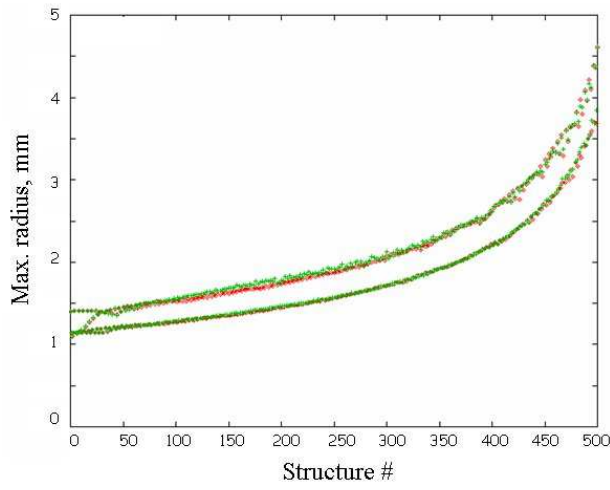
20

Figure 24: The envelopes of a $3\sigma$ beam with an initial offset of $\Delta y = 0.3\,\sigma_y$ along the decelerator with (green) and without (red) transverse wakes effects.
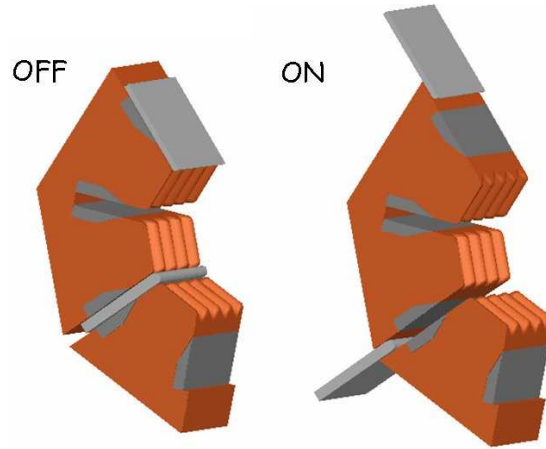


Figure 25: PETS ON/OFF configuration with detuning wedges

## 8.5 PETS "On/Off" Option

During machine operation it will be necessary to locally turn the RF power production OFF when either PETS or an accelerating structure fails due to breakdown. It can be shown that the RF power generated by the beam at the end of the constant impedance structure will be zero if the synchronous frequency is detuned by the amount $\pm\beta c/(1-\beta)L$, where $\beta = v_{\mathrm{group}}/c$ and $L$ is the length of the structure. In our case this corresponds to about 2 GHz frequency detuning. We have found that such a strong detuning can be achieved by inserting 4 thin (1.6 mm) wedges through 4 of the 8 damping slots in such a way that the edge position of the wedge does not exceed the beam aperture, see Fig. 25. The wedge geometry was modified in a way that at any intermediate wedge position there is no electrical field enhancement in the 0.2 mm gap between the wedge and the wall, nor any RF power leak in the HOM loads occur [51]. Thus the device can operate as a variable attenuator. The normalised output power level as a function of the wedge position is shown in Fig. 26.

## 9 Drive Beam Generation and Decelerator

### 9.1 Scaling Issues

As discussed before, the optimisation studies on CLIC accelerating structures have tended towards rather short structures, with a fill-time and an RF pulse length which are reduced by about a factor 2 with respect to the previous parameter set. These structures can provide RF-to-beam efficiencies equal or better than the old structures and require about the same power per meter. The main consequences of such a change on the drive beam generation complex derive from the reduction of RF pulse length. In particular, the dimensions of the delay loop and combiner rings, the number of decelerator sectors and the drive beam energy and current are linked directly to the RF pulse

21
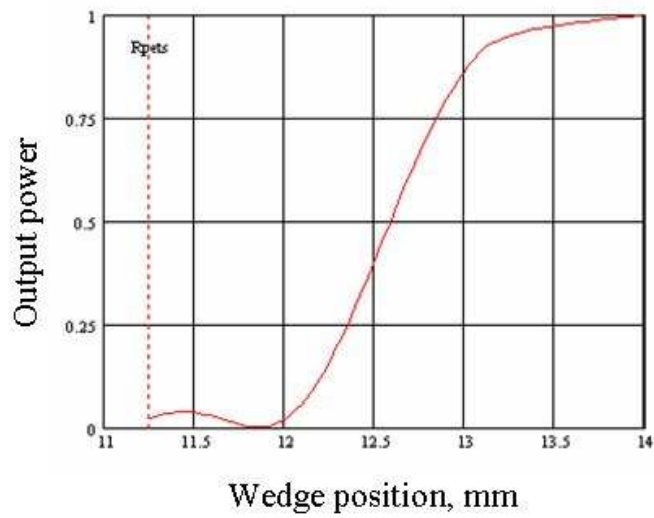
Figure 26: The normalised output power level as a function of the wedge position
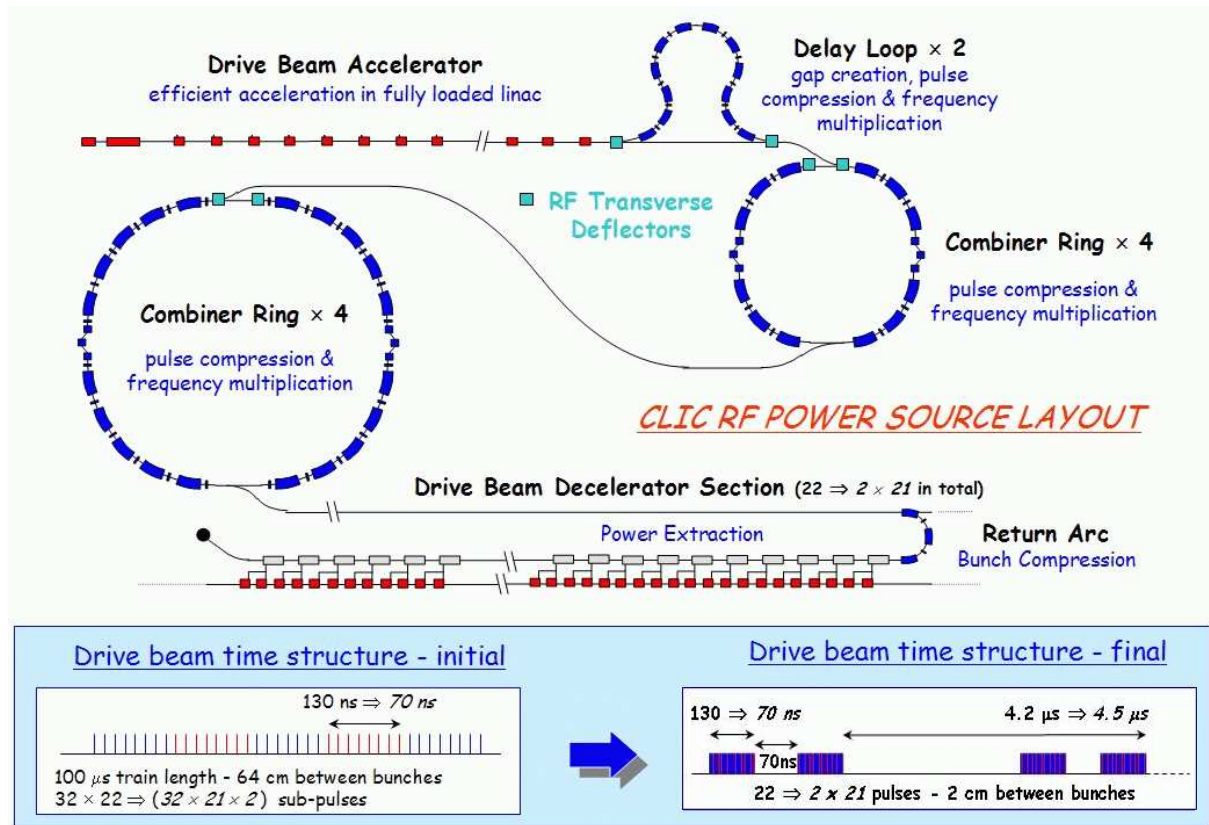


Figure 27: Schematic layout of the CLIC drive beam generation complex. The values of the new parameter set are shown in italics.

length. A general layout of the drive beam generation complex is shown in Figure 27, together with the initial and final drive beam time structure, for both the old and new parameter set.

The initial pulse length $\tau_{in} = 100\,\mu s$ corresponds to the total length of the main linac and is essentially unchanged. It depends on the final energy, the accelerating gradient and the main linac fill-factor. The length of the sub-pulses is equal to the length of the 30 GHz RF pulse $\tau_{RF}$ and must be reduced now from 130 ns to 70 ns. The combination factor $C_F$, defined as the ratio between final and initial bunch repetition frequencies and the number of decelerator sections $N_S$ link the RF pulse length to the initial pulse length as follows: $\tau_{in} = C_F \times N_S \times \tau_{RF}$. There is some freedom in the choice of the combination factor, but the final spacing between drive beam bunches (15 GHz) is

limited by the frequency of the last pair of RF deflectors (3.75 GHz) [52]. It is also preferable to use a factor four combination in each ring (rather than five, for instance), since it permits a larger septum thickness, it gives less disturbance to the circulating pulses and the setting-up with beam is simpler. A natural choice is to use two rings, for a factor $4 \times 4 = 16$, plus a delay line, needed anyway to introduce a hole in the time structure for the extraction kickers, which gives another factor 2. The total combination factor is therefore 32 and the initial frequency used for drive beam acceleration is 30 GHz/32 = 975 MHz. Such frequency represents a good compromise, since low frequencies are favourable for klystron efficiency and high peak power, while high frequencies allows for more compact accelerating structures and a shorter drive beam accelerator. For all of these reasons, it has been proposed to leave unchanged the combination factor, and the initial and final bunch spacing.

Taking into account this constraint, if the 30 GHz RF pulse length is shortened, the obvious consequence would be an increase in the number of drive beam decelerator sections and a decrease, roughly by the same factor, of the drive beam momentum. A positive consequence of that is a decrease of the energy of each drive beam pulse in the decelerator (less damage potential in case of losses). However, both cost and complexity increase, since more turn-around and dumps would be needed. With a straightforward scaling, the length of the delay line and of the rings will decrease as well. A shorter delay line would pose no problem, but a reduction in length of the first combiner ring is a problem, 78 m being already very short. The lower drive beam momentum is also a problem, since the ring impedance and Coherent Synchrotron Radiation (CSR) cause an energy spread whose absolute value does not depend on momentum. Therefore the relative energy spread would double. In reality, the drive beam momentum can be increased if the PETS impedance and the current are decreased, but the scaling of beam stability in the decelerator in this case is unfavorable.

## 9.2   The Double Pulse Scheme

Indeed, the previous drive beam parameters (10 nC/bunch, 2 GeV, beam current from 4.6 A to 150 A) were a good compromise between transverse stability in the decelerator and collective effects (wake-fields and CSR) in the DB generation complex. There is a way to stay in the same parameter space for the drive beam generation complex even with a reduced RF pulse length. This solution, called the double pulse scheme, is described in the following.

Some time ago it was proposed [53] to combine the DB generation for both e+ and e- linacs, in order to improve the DB stability in the decelerator. This can be done as follows:

- Use a single accelerator with double length, doubling the beam momentum,
- keep unchanged the initial pulse length, and the length of the delay line and combiner rings,
- switch subsequent pulses to power the e+ and e- main linacs, thus doubling the distance between pulses in each decelerator,
- half the number of decelerator sectors.

In the case of a reduced RF pulse, it is possible to use a single drive beam generation complex to feed both linacs, in a different way:

- keep one "long" linac as for the long RF pulse,
- use a "short" delay loop (21 m for 70 ns),
- use "long" combiner rings (84 m and 334 m for 70 ns),
- in each ring two pulses will circulate and will be combined at the same time,
- the combined pulse pairs can be separated and sent to the $e^+$ and $e^-$ main linacs.

The proposed method is schematically described in Figure 28. By using this method, the number of decelerator sections is kept small (21) and the drive beam energy is high (2.4 GeV).

The main hardware changes are the reduction of the delay line length and the need of a kicker after extraction from the second combiner ring, to switch every second pulse from the electron to the positron linac. The main issue left is the drive beam energy, increased by 20% with respect to the old parameter set. Possible limitations come from the increased field in the combiner ring magnets and from an increase in synchrotron radiation losses.

By scaling directly the ring design proposed in [54], reasonable values of the magnetic field are obtained for all magnets, except for the main dipoles of the first ring, which would need an on-axis field of 2.2 T. A small , increase of the dipole fill factor of the ring, which is about 27%, would however reduce the field below a more conservative value of 2 T. This can be easily obtained, for instance, by modifying the isochronous cell lattice from a four-bends to a three-bends solution [55]. In the following a fill factor increased by about 20% is assumed for both rings. In Figure 29, the total relative energy loss for bunches making the maximum number of turns in both rings is pictured as a function of the drive beam momentum. For a momentum of 2.4 GeV, the maximum relative energy loss is about 0.1%, which is acceptable for beam dynamics.

The energy loss is dominated in this case by incoherent synchrotron radiation effects. CSR losses are small thanks also to the shielding effect of the vacuum chamber. The power lost by synchrotron radiation by the high current drive beam is however not negligible. The average power loss is about 7 kW/m in the first ring dipoles and 250 W/m

23
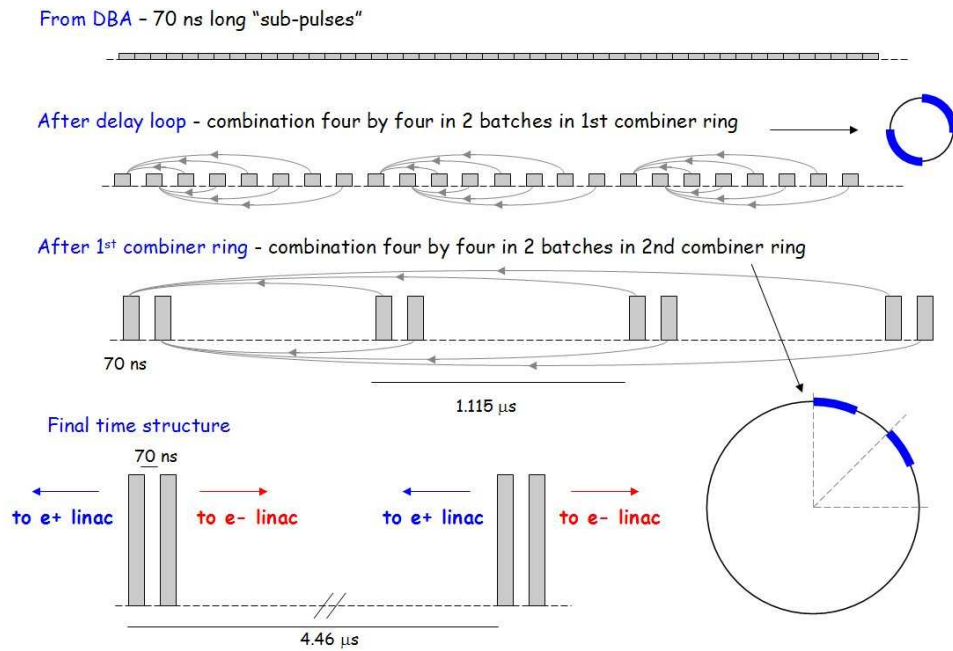
Figure 28: Schematic description of the proposed time structure evolution of the drive beam during the combination process.
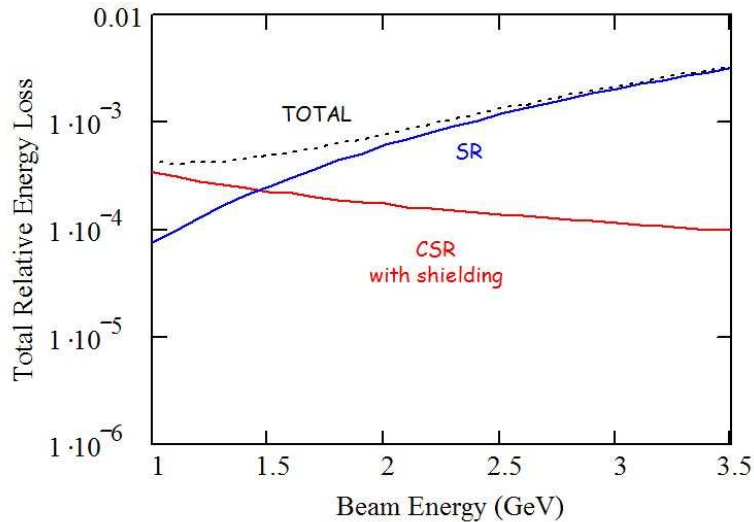


Figure 29: Total relative energy loss from synchrotron radiation, both coherent and incoherent, as a function of beam momentum. The contribution of both rings is taken into account.

in the dipoles of the second ring, and its absorption and cooling is not a trivial problem. On the other hand, the increase in beam emittance and energy spread caused by the incoherent emission are negligible ($\delta\epsilon/\epsilon < 1\%$, $\sigma_p/p \simeq 3 \times 10^{-5}$). Finally, the increase in momentum doesn't affect the RF power needed in the ring deflectors; the real emittance adiabatic damping implies that a smaller kick is needed, compensating to first order the increase in power for a fixed kick strength.

## 9.3 DBA Accelerating Structures

For the new parameters and layout from the previous section, the drive beam accelerator (DBA) will consist of 176 accelerating structures, each of 28 cells and approximately 3.5 m length. It will operate in $2\pi/3$ mode, fully beam loaded by a beam current of 5.7 A and it will have a moderate accelerating gradient of 3.9 MV/m. The unloaded gradient is 7.4 MV/m. This will bring the drive beam to 2.37 GeV.
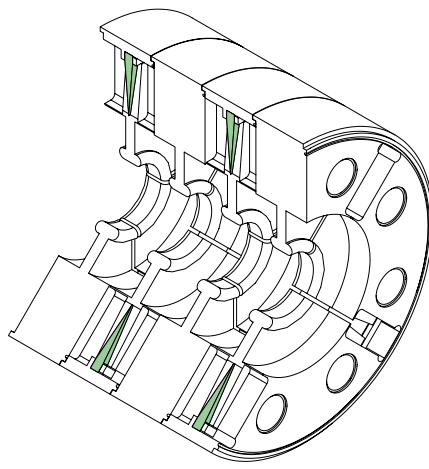
Figure 30: Conceptual view of the SICA accelerating structure.
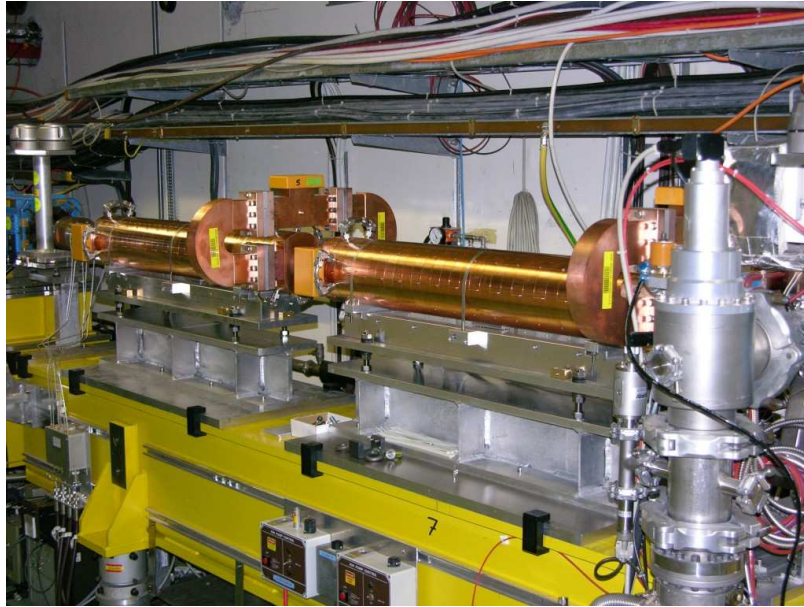


Figure 31: Two 3 GHz SICA structures during installation in CTF3.

Two types of structures have been studied [56]: the "Tapered Damped Structure" (TDS), originally designed for the CLIC main accelerator and downscaled by a factor 32. Dipole mode damping in TDS is attained by coupling SiC loads through 4 waveguides to the accelerating cavities. The cut-off frequency of these waveguides is chosen above the operating frequency, but below the higher order mode frequencies. It thus serves as a high-pass filter between the cavity and the dampers. A TDS scaled to 937 MHz would however be very large (outer diameter 1.4 m).

The impractical size of TDS was one of the reasons to study in detail a novel type of structure [57]. The SICA structure (for "Slotted Iris - Constant Aperture") has 4 radial slots in each iris, which virtually do not perturb the fundamental mode field. Dipole mode currents however are intercepted by the slots. The slots continue radially into ridged waveguides which contain tapered SiC loads. These are designed so as to drastically reduce the $Q$ of the dipole modes (to values typically below 20). As opposed to TDS, where the higher order modes are separated by a filter from the accelerating mode, mode separation in SICA uses the geometric differences and special symmetries of the mode patterns. SICA structures were successfully built and tested at 3 GHz and are being implemented as DBA structures for CTF3. At 937 MHz, SICA structures would have an outer diameter of approximately 550 mm. Fig. 30 shows an artists conception of the accelerating structure, Fig. 31 shows a photograph of two 3 GHz SICA structures during installation in CTF3.

Another feature of the SICA structures is the constant iris aperture which reduces the short range wakes. The detuning is obtained by introducing nose cones with varying depths. These nose cones lead to a larger ratio of surface field to accelerating gradient in the downstream cells (ratio of up to 3.4), but this is acceptable since the

| | 3 GHz DBA | | | 937 MHz DBA | | | unit |
|---|---|---|---|---|---|---|---|
| operating frequency | 2998.55 | | | 937.05 | | | MHz |
| beam current | 3.5 | | | 5.7 | | | A |
| | 1st cell | center cell | last cell | 1st cell | center cell | last cell | |
| cavity diameter | 82.95 | 79.00 | 74.39 | 265.44 | 252.80 | 238.05 | mm |
| nose cone size | 0.00 | 2.53 | 4.66 | 0.00 | 8.10 | 14.91 | mm |
| iris thickness | 6.00 | | | 19.20 | | | mm |
| iris diameter | 34.00 | | | 108.80 | | | mm |
| phase advance/cell | 120 ° | | | 120 ° | | | |
| $r'/Q$ (Linac $\Omega$) | 3143 | 3292 | 3165 | 982 | 1029 | 989 | $\Omega$/m |
| group velocity | 5.19 | 3.49 | 2.36 | 5.19 | 3.49 | 2.36 | % $c$ |
| $Q$ accelerating mode | 13860 | 12771 | 10950 | 24794 | 22845 | 19588 | |
| frequency 1st dipole | 4147 | 4197 | 4097 | 1296 | 1314 | 1279 | MHz |
| kick factor 1st dipole | 555 | 668 | 843 | 16.95 | 20.22 | 5.90 | V/pC/m² |
| $Q$ 1st dipole mode | 17.5 | 6.2 | 5.8 | 17.5 | 6.2 | 5.7 | |
| frequency 2nd dipole | 4243 | 4279 | 4379 | 1326 | 1318 | 1335 | MHz |
| kick factor 2nd dipole | 206 | 254 | 197 | 6.29 | 8.07 | 25.00 | V/pC/m² |
| $Q$ 2nd dipole mode | 3.4 | 17.3 | 24.4 | 3.4 | 3.4 | 3.4 | |
| cell length | 33.32 | | | 106.62 | | | mm |
| number of cells/structure | 32 | | | 28 | | | |
| structure length | 1.22 | | | 3.48 | | | m |
| fill time, $\tau$ | 98 | | | 278 | | | ns |
| input power | 30 | | | 80 | | | MW |
| accelerating voltage, unloaded | 13.3 | | | 25.7 | | | MV |
| accelerating voltage, loaded | 7.9 | | | 13.5 | | | MV |
| beam loading, $\kappa$ | 97.4 | | | 99.0 | | | % |
| efficiency, $\eta$ | 92.5 | | | 96.0 | | | % |
| number of structures | 2+16 | | | 2+176 | | | |
| total energy gain | 127 | | | 2376 | | | MeV |

Table 7: Parameters of the DBA accelerating structures.

overall accelerating gradient is moderate.

Issues which were addressed in the design were *i)* the field enhancement at the slot edges and *ii)* the presence of low frequency "slot modes" and their potential impact on the performance. The field enhancement is reduced to acceptable 40% by a modest rounding of the edges (rounding radius of approximately half the slot width). This additional field enhancement will lead to a maximum surface field of 33 MV/m or 1.2 Kilpatrick at the slot edges in the last cell.

The slot modes, which occur at frequencies of about 2/3 of the operating frequency, have the electric field across the slots and are strongly damped ($Q < 6$) if the cut-off frequency of the ridged waveguide is chosen low enough. The kick factor of the slot mode is found to be at an acceptable 5% of that of the lowest dipole mode.

A total of 18 SICA structures operating at 3 GHz have been built by industry [58]. They are installed in CTF3 and have been successfully operated at and above their specification during 2003 and 2004. The CTF3 drive beam linac is now operated routinely under full beam-loading condition [59].

The parameters of the DBA accelerating structures are summarised in Table 7.

## 10 Overall Layout, Efficiency and AC Power Consumption

Figure 32 shows the overall CLIC layout resulting from the new parameters, the newly introduced train combination scheme after the damping rings for the main beam and the modified drive beam production scheme.

The efficiencies for the different subsystems have been recalculated with the updated parameters. One modification to the old parameter set is the assumption of a klystron efficiency of 70% (instead of 65%). This value was changed since Multi Beam Klystrons are expected to obtain efficiencies well above 70% and a value close to 70% was already experimentally demonstrated [60].

Table 8 shows the total AC power resulting from the power consumption of the drive beam accelerator and various components in the tunnel and the central injector complexes. The latter numbers have been adapted from [4] since
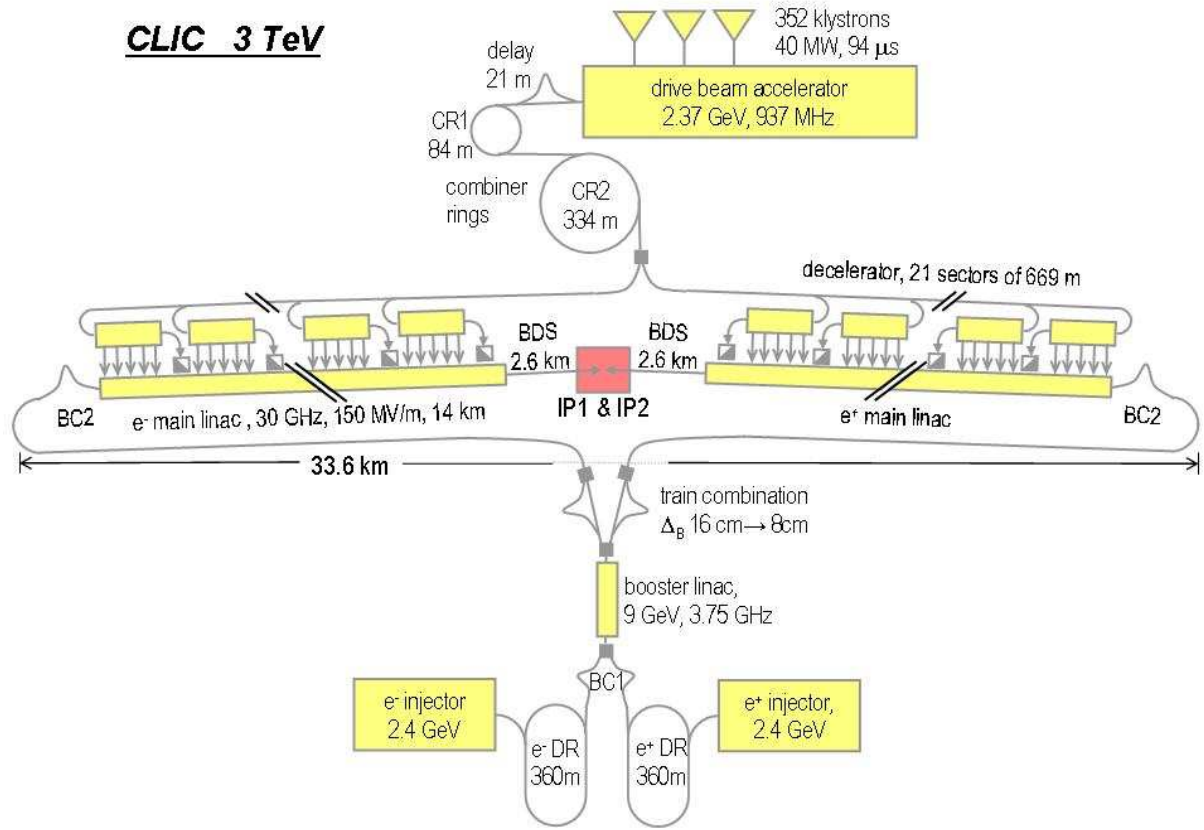
Figure 32: CLIC layout with train combination scheme after the damping rings and the modified drive beam production.

|  | unit | old | new |
|---|---|---|---|
| $P_{\text{AC DB-acc.}}$ | MW | 311 | 322 |
| Main beam injectors | MW | 7 | 7 |
| Central area magnets/services/detectors | MW | 35 | 35 |
| Tunnel services and magnets | MW | 25 | 25 |
| DB-acc. reliability margin (klystron failure) | MW | 24 | 25 |
| Modulator auxiliaries | MW | 4 | 4 |
| $P_{\text{AC Total}}$ | MW | 406 | 418 |
| $P_{\text{main beams}}$ (sum of both) | MW | 31.1 | 40.6 |
| $\eta_{\text{tot}}\ (= P_{\text{main beams}}/P_{\text{AC Total}})$ | % | 7.7 | 9.7 |
| $\mathcal{L}_1$ | $10^{34}\text{cm}^{-2}\text{s}^{-1}$ | 3.3 | 3.3 |
| $\mathcal{L}_1/P_{\text{AC total}}$ | $10^{34}\text{cm}^{-2}\text{s}^{-1}\text{MW}^{-1}$ | 8.1 | 7.9 |

Table 8: Power consumption for the various components and efficiency.

no important changes affecting these numbers have been performed. It is worth mentioning that the overall power consumption has stayed almost constant despite the substantial improvement in RF power to beam power efficiency of the main beam. The reason is that the accelerating structure design optimisation resulted in a smaller bunch charge, which drives us further away from the advantageous regime of $\mathcal{L} \sim P_{\text{beam}}/\sqrt{\sigma_z}$ as already mentioned in section 1.

The power flow from the wall plug to the main beams power with the corresponding efficiencies is illustrated in Fig. 33. A expected total efficiency $\eta_{\text{tot}}$ is therefore 9.7%.

Overall, a major update of the CLIC design and 3 TeV parameters has been undertaken, including many new developments. These new parameters comply with our present knowledge on RF breakdown limits. The present
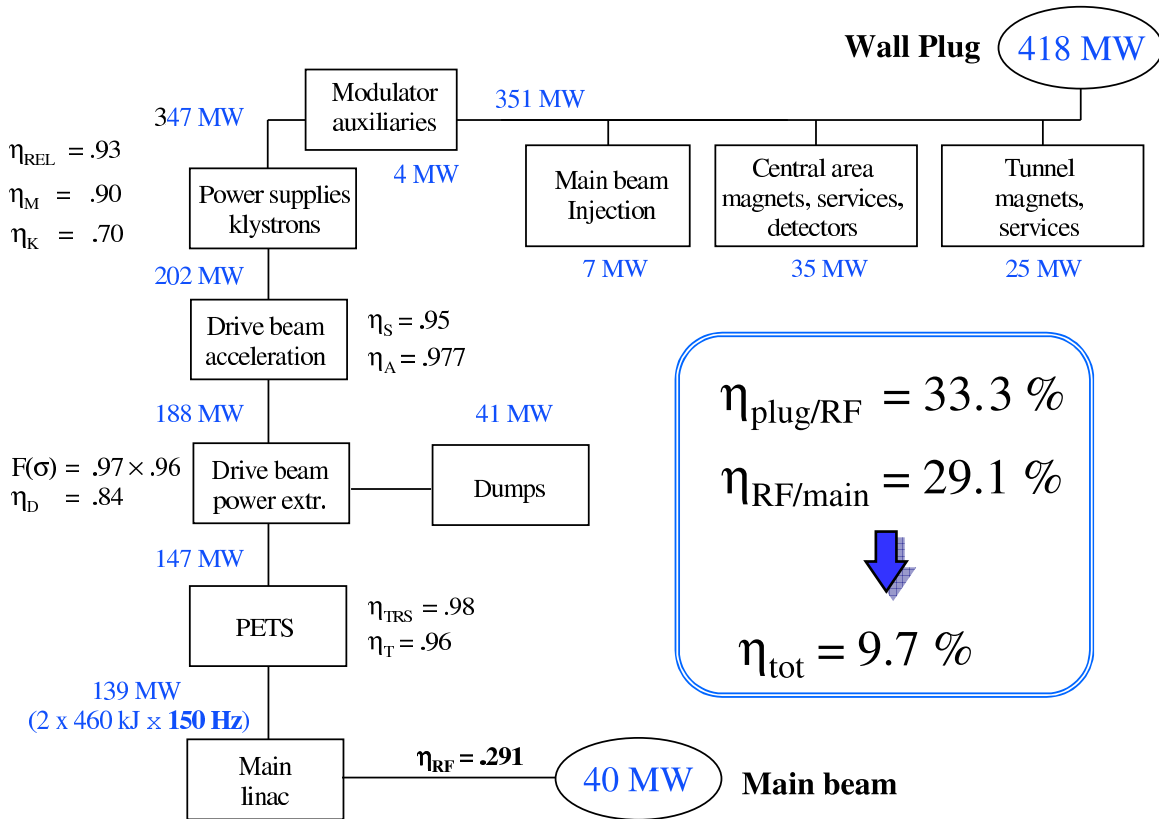
Figure 33: Power flow diagram with component efficiencies.

design has achieved similar effective luminosity, total power consumption and total length as in the previous design, while the RF to beam power efficiency has been increased and the IP backgrounds have been reduced.

## 11 Parameters for 1 TeV Centre of Mass Energy

Possible parameters for a machine with a centre-of-mass energy of 1 TeV can be derived from the ones for 3 TeV. In order to reach $E_{cm} = 1$ TeV, seven rather than 21 drive beam sectors are necessary per linac. Consequently, the pulse length of the drive beam can be reduced by a factor of three.

The main beam generation complex will remain unchanged as will the accelerating gradient in the main linac. The linac lattice is based on the first third of the one for the 3 TeV machine and the emittance budget is kept at the same level. Consequently all beam parameters will remain unchanged at the entrance of the beam delivery system. The target beta-functions at the interaction point are 10 mm in the horizontal and 0.1 mm in the vertical plane. This would lead to a luminosity of $3.8 \times 10^{34}$ cm$^{-2}$s$^{-1}$. The average energy loss of $\Delta E/E \approx 10\%$ due to beamstrahlung remains quite acceptable and the luminosity spectrum is of good quality since less than one beamstrahlung photon is emitted on average per beam particle. No specific design of the beam delivery system has been developed but the lattice for 3 TeV has been used, modifying the strength of all magnets to follow the beam energy. The main beam parameters at the interaction point, the luminosity and background figures are given in Table 9 for the linear design and the results from particle tracking. As can be seen, the luminosity from tracking is lower than anticipated from the beta-functions. A re-optimisation of the lattice for 1 TeV would very likely improve the luminosity performance.

| Parameter | Design | Tracking |
|---|---|---|
| $N [10^9]$ | 2.56 | 2.56 |
| $N_b$ | 220 | 220 |
| $f_{\mathrm{rep}}$ [Hz] | 150 | 150 |
| $\sigma_z$ [$\mu$m] | 30.8 | 30.8 |
| $\epsilon_x/\epsilon_y$ [nm] | 660/10 | 660/10 |
| $\beta_x/\beta_y$ [mm] | 10/0.1 | 10/0.1 |
| $\sigma_x/\sigma_y$ [nm] | 82/1 | 94/1 |
| $L$ [$10^{34}$cm$^{-2}$s$^{-1}$] ($L_{0.01}/L$ [%]) | 3.8 (60) | 2.8 (61) |
| $N_{\mathrm{coh}}$ [$10^6$] | 0.9 | 0.6 |
| $N_{\mathrm{had}}/N_{pt}$ | 0.25/13 | 0.17/10 |
| $\Delta E$ [%] ($N_\gamma$) | 10 (1.0) | 9 (0.9) |

Table 9: Beam parameters at the interaction point of CLIC at 1 GeV centre-of-mass energy. The results for a perfect beam delivery system (design) and one from tracking through a BDS with a simple scaling of the current 3 TeV design (tracking) are shown.

**Appendix**

**A    Tables of Parameters**

| *Parameter* | *Symbol* | *Value* | *Unit* |
|---|---|---|---|
| ***Overall Parameters*** | | | |
| Centre of mass energy | $E_{\mathrm{CMS}}$ | 3000 | GeV |
| Main Linac RF Frequency | $f_{\mathrm{rf}}$ | 30 | GHz |
| Luminosity | L | 6.5 | $10^{34}$cm$^{-2}$s$^{-1}$ |
| Luminosity (in 1% of energy) | $L_{99\%}$ | 3.3 | $10^{34}$cm$^{-2}$s$^{-1}$ |
| Linac repetition rate | $f_{rep}$ | 150 | Hz |
| No. of particles / bunch | $N$ | 2.56 | $10^9$ |
| No. of bunches / pulse | $N_b$ | 220 | |
| Bunch separation | $\Delta t_b$ | 0.267 (8 periods) | ns |
| Bunch train length | $\tau_{\mathrm{train}}$ | 58.4 | ns |
| Beam power / beam | $P_b$ | 20.3 | MW |
| Unloaded / loaded gradient | $G_{\mathrm{unl/l}}$ | 172 / 150 | MV/m |
| Overall two linac length | $l_{\mathrm{linac}}$ | 28 | km |
| Total beam delivery length | $l_{\mathrm{BD}}$ | 2 x 2.6 | km |
| Proposed site length | $l_{\mathrm{tot}}$ | 33.2 | km |
| Total site AC power | $P_{\mathrm{tot}}$ | 418 | MW |
| Wall plug to main beam power efficiency | $\eta_{tot}$ | 9.7 | % |

Table 10: Overall parameters

| Parameter | Symbol | Value | Unit |
|---|---|---|---|
| **Main Linac** | | | |
| Overhead for energy fdbk & repair | $\text{ovh}_{\text{rep}}$ | 5 | % |
| Overhead for off-crest operation | $\text{ovh}_{\text{off-crest}}$ | 5 | % |
| Acceleration structure length (active/full) | $l_{\text{struct}}$ | 0.233 / 0.243 | m |
| average $\langle a/\lambda \rangle$ | $a/\lambda$ | 0.178 | |
| Group velocity | $v_g/c$ | 12.2 - 5.07 | % |
| Filling time | $\tau_f$ | 9.5 | ns |
| Unloaded Quality factor | Q | 2590 - 2244 | |
| Shunt impedance (first/last cell) | $r_s$ | 79 / 92 | (Linac)M$\Omega$/m |
| RF -> main beam efficiency | $\eta_{b,\text{RF}}$ | 29.1 (Mo) | % |

Table 11: Main linac and accelerating structure parameters

| Parameter | Symbol | Value | Unit |
|---|---|---|---|
| **Main Beam in damping ring before extraction** | | | |
| Energy | $E_{b,\text{DR}}$ | 2.424 | GeV |
| No. of particles / bunch | $N_b$ | 2.56+5% | $10^9$ |
| Bunch length | $\sigma_{s,\text{DR}}$ | 1550 | mm |
| Energy spread | $\sigma_E/E_{\text{DR}}$ | 0.13 | % |
| Transverse horizontal emittance | $\gamma\varepsilon_{x,\text{DR}}$ | 550 | nm rad |
| Transverse vertical emittance | $\gamma\varepsilon_{y,\text{DR}}$ | 3.3 | nm rad |
| Longitudinal emittance (normalised) | | 4700 | eVm |
| | | | |
| **Electron / positron damping ring** | | | |
| Ring circumference | $C_{\text{DR}}$ | 360 | m |
| Number of trains stored | $n_{\text{train}}$ | 4 | |
| Number of bunches / train | $N_b$ | 110 | |
| Bunch separation | $\Delta t_{b,\text{DR}}$ | 0.533 | ns |
| RF frequency | $f_{\text{DR}}$ | 1875 | MHz |
| Wiggler length | $l_{\text{wig}}$ | 152 | m |
| Damping times | $\tau_x$ / $\tau_y$ / $\tau_z$ | 2.8 / 2.8 / 1.4 | ms |
| Tunes | $Q_x$/ $Q_y$ | 69.82 / 34.86 | |
| | | | |
| **Main Beam at linac injection** | | | |
| Energy | $E_{b,\text{inj}}$ | 9 | GeV |
| No. of particles / bunch | $N_b$ | 2.56 | $10^9$ |
| Bunch length | $\sigma_{s,\text{inj}}$ | 30.8 | $\mu$m |

Table 12: Main Beam and damping ring parameters

| Parameter | Symbol | Value | Unit |
|---|---|---|---|
| **Beam Delivery System + IP** | | | |
| Total collimation system length | $l_{\mathrm{coll}}$ | 2 x 2.05 | km |
| Total final Focus system length | $l_{\mathrm{FF}}$ | 2 x 0.55 | km |
| Input transverse horizontal emittance | $\varepsilon_x$ | 660 | nm rad |
| Input transverse vertical emittance | $\varepsilon_y$ | 10 | nm rad |
| Nominal horizontal IP beta function | $\beta_x^*$ | 7 | mm |
| Nominal vertical IP beta function | $\beta_y^*$ | 0.09 | mm |
| Horizontal IP core beam size | $\sigma_x^*$ | 60 | nm |
| Vertical IP core beam size | $\sigma_y^*$ | 0.7 | nm |
| Bunch length | $\sigma_{s,\mathrm{inj}}$ | 30.8 | $\mu$m |
| Initial RMS Energy spread | $\sigma_{\Delta E/E}^*$ | 0.35 | % |
| Total Energy spread | | 1 | % |
| Crossing angle at IP | $\theta_C$ | 20 | mrad |
| Disruptions | $\mathrm{D}_x$ / $\mathrm{D}_y$ | 0.04 / 3.5 | |
| Beamstrahlung mom. spread | $\delta_B$ | 16 | % |
| No. of photons / electron | $n_\gamma$ | 1.1 | |
| No. of pairs ($p_T^{\mathrm{min}}$=20MeV/c, $\theta_{\mathrm{min}}$=0.2) | $N_{\mathrm{pairs}}$ | 17.4 | $10^7$ |
| No. of coherent pairs / bunch crossing | $N_{\mathrm{coh}}$ | 5 | $10^7$ |
| Hadronic events / crossing | $N_{\mathrm{hadron}}$ | 0.73 | |
| No. of jets ($p_T^{\mathrm{min}}$=3.2 GeV/c) | $N_{\mathrm{jets}}$ | 0.52 | |
| Geometric luminosity | $L_{\mathrm{geom}}$ | 4.1 | $10^{34}\mathrm{cm}^{-2}\mathrm{s}^{-1}$ |
| Peak luminosity (ideal) | $L_{\mathrm{pk}}$ | 6.5 | $10^{34}\mathrm{cm}^{-2}\mathrm{s}^{-1}$ |
| Luminosity (in 1% of energy) | $L_{99\%}$ | 3.3 | $10^{34}\mathrm{cm}^{-2}\mathrm{s}^{-1}$ |

Table 13: Beam Delivery System, IP and background parameters

| Parameter | Symbol | Value | Unit |
|---|---|---|---|
| **Decelerator** | | | |
| No. of drive beam sectors / linac | $N_S$ | 21 | |
| Unit length (total) | $l_{\mathrm{unit}}$ | 669 | m |
| Average fill factor | F | 50.1 | % |
| No. of PETS / sector | $N_{\mathrm{PETS,unit}}$ | 559 | |
| Length of PETS (active/overall) | $l_{\mathrm{PETS}}$ | 0.6 / 0.77 | m |
| Nominal output RF Power / PETS | $P_{\mathrm{out}}$ | 642 | MW |
| Transfer efficiency PETS > HDS | | 94 | % |
| Number of accelerating structures / PETS | | 4 | |
| Main beam acceleration power / PETS | $P_{\mathrm{acc}}$ | 4 x 151 | MW |
| Main beam energy gain / unit | $\Delta E_{\mathrm{main}}$ | 71 | GeV |
| drive beam -> RF efficiency (HDS input) | $\eta_{\mathrm{decRF}}$ | 74 | % |

Table 14: Decelerator and PETS parameters

| Parameter | Symbol | Value | Unit |
|---|---|---|---|
| **Drive beam basic parameters** | | | |
| Energy (decelerator injection) | $E_{\mathrm{in,dec}}$ | 2.37 | GeV |
| Energy (final, minimum) | $E_{\mathrm{fin,dec}}$ | 237 | MeV |
| Average current in pulse | $I_{\mathrm{dec}}$ | 181 | A |
| Train duration | $\tau_{\mathrm{train}}$ | 69.7 | ns |
| No. bunches / train | $N_{b,\mathrm{dec}}$ | 1046 | |
| Bunch charge | $Q_{b,\mathrm{dec}}$ | 12.1 | nC |
| Bunch separation | $\Delta_{b,\mathrm{dec}}$ | 0.067 | ns |
| Bunch length, rms | $\sigma_{s,\mathrm{dec}}$ | 0.4 | mm |
| Normalised emittance, rms | $\gamma\varepsilon_{\mathrm{dec}}$ | 150 | $\mu$m rad |
| | | | |
| **Drive Beam linac** | | | |
| RF frequency | $f_{\mathrm{RF}}$ | 937 | MHz |
| Total number of klystrons | $N_{\mathrm{kly}}$ | 2 * 176 | |
| Klystron peak power | $P_{\mathrm{kly}}$ | 40 | MW |
| Repetition frequency | $f_{\mathrm{rep}}$ | 150 | Hz |
| Beam energy | $E_{\mathrm{DB}}$ | 2.37 | GeV |
| Pulse length (total train) | $\tau_{\mathrm{pulse}}$ | 93.7 | $\mu$s |
| Beam current per pulse | $I_{\mathrm{DB}}$ | 5.7 | A |
| Charge per pulse | $Q_{\mathrm{pulse}}$ | 530 | $\mu$C |
| Number of bunches / pulse | $N_{b,\mathrm{pulse}}$ | 43932 | |
| Bunch length (rms) | $\sigma_s$ | 4 | mm |
| Normalised emittance (at injection) | $\gamma\varepsilon_i$ | 100 | $\mu$m rad |
| Total energy spread (at injection) | $\Delta$E/E | 1 | % |
| RF -> drive beam efficiency | $\eta_{b,\mathrm{RF}}$ | 93 | % |

Table 15: Drive Beam parameters

| Parameter | Symbol | Value | Unit |
|---|---|---|---|
| **Delay Line** | | | |
| Length | $L_D$ | 21 | m |
| RF deflector frequency | $f_D$ | 468 | MHz |
| Combination factor | $F_{C,D}$ | 2 | |
| Bunch length (rms) | $\sigma_s$ | 2 | mm |
| | | | |
| **Combiner Ring 1** | | with 2 trains | |
| Length | $L_{R1}$ | 84 | m |
| RF deflector frequency | $f_{R1}$ | 937 | MHz |
| Combination factor | $F_{C,R1}$ | 4 | |
| Bunch length (rms) | $\sigma_s$ | 2 | mm |
| | | | |
| **Combiner Ring 2** | | with 2 trains | |
| Length | $L_{R2}$ | 334 | m |
| RF deflector frequency | $f_{R2}$ | 3750 | MHz |
| Combination factor | $F_{C,R2}$ | 4 | |
| Bunch length (rms) | $\sigma_s$ | 2 | mm |

Table 16: Delay Line and Combiner Ring parameter

# References

[1] presentations at "Workshop on High Gradient RF", ANL 2003, http://www.mice.iit.edu/rfworkshop/

[2] D. Schulte, "Luminosity Limitations at the Multi TeV Linear Collider Energy Frontier," Proc. EPAC 2002 and CLIC Note 527 (2002)

[3] J.Y. Raguin, I. Wilson, W. Wuensch, "Progress in the Design of a Damped and Tapered Accelerating Structure for CLIC", Proc. PAC 2003 and CLIC Note 567 (2003)

[4] G. Guignard (editor), "CLIC Contribution to the Technial Review Committee on a 500 GeV e+e- Linear Collider", CERN report 2003-7

[5] A. Grudiev, W. Wuensch, "A Newly Designed and Optimized CLIC Main Linac Accelerating Structure", Proc. LINAC 2004 and CLIC Note 601 (2004)

[6] M. Battaglia, A. de Roeck, J. Ellis, D. Schulte (editors), "Physics at the CLIC Multi-TeV Linear Collider : report of the CLIC Physics Working Group", CERN report 2004-005, hep-ph/0412251

[7] J.P. Delahaye, G. Guignard, T. Raubenheimer and I. Wilson, "Scaling Laws for e+/e- Linear Colliders", CLIC Note 333 (1997)

[8] H.H. Braun, D. Schulte, "Optimum Choice of RF Frequency for Two Beam Linear Colliders", CLIC Note 563 (2003)

[9] W. Wuensch, H. Braun, S. Doebert, I. Syratchev, and I. Wilson, "A Demonstration of High-Gradient Acceleration", PAC'03, CLIC Note 569 (2003)

[10] S.T. Heikkinen , S. Calatroni, H. Neupert, "Thermal fatigue issues in high gradient particle accelerators", 6$^{th}$ international congress on thermal stresses, 26-29 May, 2005, Vienna, AUSTRIA

[11] V. Dolgashev, "Effect of Rf Magnetic Fields and Input Power on Rf Breakdown Limit", Workshop on High-Gradient RF, Argonne, October 2003

[12] M. Korostelev, F. Zimmermann, "Optimization of the CLIC Damping Ring Design Parameters", EPAC'02, Paris, 3–7 June 2002, CLIC Note 518 (2002)

[13] M. Korostelev, F. Zimmermann, "A Lattice Design for the CLIC Damping Ring", Nanobeam'02 ICFA Workshop, Lausanne, 1–6 September 2002, CLIC Note 558 (2002)

[14] K.L.F. Bane, "A Simplified Model of Intrabeam Scattering", EPAC 2002 Paris (2002)

[15] A. Piwinski, in Handbook of Accelerator Physics, World Scientific (1999), A. Chao and M. Tigner (eds.), p. 125

[16] K. Brown, "A Second Order Magnetic Optical Achromat", SLAC-PUB-2257 (1979)

[17] M. Korostelev, F. Zimmermann, "Nonlinear Optimization of a Low-Emittance CLIC Damping Ring Lattice", PAC2003, Portland, 12–16 May, 2003, CLIC Note 564 (2003)

[18] R. Brinkmann, Ya. Derbenev, K. Flottmann, "A Low Emittance Flat-Beam Electron Source for Linear Colliders", Phys. Rev. ST. Accel. Beams 4, 053501 (2001)

[19] M. Korostelev, J. Wenninger, F. Zimmermann, "Flexibility, Tolerances, and Beam-Based Tuning of the CLIC Damping Ring", EPAC'04, Lucerne, 5–9 July, 2004, CLIC Note 605 (2004)

[20] M. Korostelev, D. Schulte, F. Zimmermann, T. Agoh, K. Yokoya, "Collective Effects in the CLIC Damping Rings", PAC'2005, Knoxville, CLIC Note 632 (2005)

[21] D. Schulte, R. Wanzenberg, F. Zimmermann, "Electron-Cloud Effects in the TESLA and CLIC Positron Damping Rings", Proc. ECLOUD'04, Napa, 2004, CERN-2005-001 (2005)

[22] H. Braun, M. Korostelev, F. Zimmermann, "Potential of Non-Standard Emittance Damping Schemes for Linear Colliders", APAC'04, Gyeongju, 2004, CLIC Note 594 (2004)

[23] L. Rinolfi, "A CLIC injector complex for the main beams", CLIC Note 354 (1998)

[24] T. Kamitani and L. Rinolfi, "Positron Poduction for CLIC", CLIC Note 465 (2000)

[25] A. Ferrari, L. Rinolfi, F. Tecker, "Design Study of the CLIC Main Beam Injector Linac," CLIC Note 626 (2005)

[26] http://www.eutotev.org

[27] T.E. D'Amico, G. Guignard, T. Raubenheimer, "The CLIC Main Linac Linac Bunch Compressor", EPAC'98, Stockholm, Sweden, CLIC Note 372, CERN/PS/98-020 (LP)

[28] D. Schulte, "Emittance Preservation in the Main Linac of CLIC", EPAC'98, Stockholm, Sweden, CLIC Note 370, CERN/PS/98-018 (LP)

[29] M. Aleksa et al., "CLIC Beam Delivery System", Nanobeam'02 ICFA Workshop, Lausanne, 2–6 September, 2002, CLIC Note 551 (2002)

[30] R. Assmann et al., "Collimation for CLIC", HALO'03 Workshop, Montauk, 19–23 May, 2003, CLIC Note 579 (2003)

[31] P. Tenenbaum, "Studies of Beam Optics and Scattering the Next Linear Collider Post-Linac Collimation System", LINAC2000 Monterey (2000)

[32] D. Schulte, F. Zimmermann, "Failure Modes in CLIC", PAC01, Chicago, CLIC Note 492 (2001)

[33] P. Raimondi and A. Seryi, "A Novel Final Focus Design for Future Linear Colliders", Phys. Rev. Let. 86, 3779 (2001)

[34] F. Zimmermann, R. Assmann, G. Guignard, D. Schulte, O. Napoly, EPAC 2000 Vienna, CLIC Note 446 (2000)

[35] F. Zimmermann, H. Burkhard, T. Risselada, F. Schmidt, H.-J. Schreiber, "Final Focus Schemes for CLIC at 3 TeV", HEACC'01 Tsukuba, CLIC Note 476 (2001)

[36] S. Redaelli et al., "Comparative Assessment of Simulation Tools for Beam Delivery Systems of Linear Colliders", Nanobeam'02 ICFA Workshop, Lausanne, 2–6 September, 2002, CLIC Note 577 (2002)

[37] D. Schulte, at CLIC Parameter Meeting, April 2005

[38] D. Schulte, F. Zimmermann, "Phase and Amplitude Tolerance in the CLIC Main Linac", CLIC Note 588 (2003)

[39] O. Napoly, "CLIC 3-TeV Interaction Region and Final-Focus Studies", CLIC Note 414 (1999)

[40] F. Zimmermann, "Quantum Mechanical Limits on Beam Demagnification and Luminosity", Nanobeam'02 ICFA Workshop, Lausanne, 2–6 September, 2002

[41] T. Markiewicz and A. Seryi, LCWS'04 Paris (2004)

[42] S. Fartoukh, B. Jeanneret, J. Pancin, "Heat Deposition by Transient Beam Passage in Spoilers", CERN-SL-2001-012 AP (2001)

[43] S. Redaelli, "Stabilization of Nanometre-Size Particle Beams in the Final Focus System of the Compact LInear Collider (CLIC)", Ph.D. thesis U. Lausanne, CLIC Note 595 (2004)

[44] C. Adolphsen et al., "Zeroth-Order Design Report for the Next Linear Collider", Volume II, p. 692 (1996)

[45] The CLIC Study Team (edited by G. Guignard), "A 3 TeV e+/e- Linear Collider Based on CLIC Technology", CERN Report 2000-008

[46] I. Syratchev, "Efficient RF Power Extraction from the CLIC Power Extraction and Transfer Structure (PETS)", CLIC Note 571 (2003)

[47] HFSS, http//www.ansoft.com/products/hf/hfss/

[48] W. Bruns, I. Syratchev, "Time Domain Simulations of the CLIC PETS with GdfidL", PAC01, Chicago, June 2001, CLIC Note 490 (2001)

[49] D. Schulte, CERN/PS 2000-028 AE, (2000)

[50] D. Schulte and I. Syratchev, "Considerations on the Design of the Decelerator of the CLIC Test Facility (CTF3)", PAC2005, May 2005, CLIC Note 634 (2005)

[51] I. Syratchev, "The CLIC Power Extraction and Transfer Structure (PETS)", CLIC Meeting 03.12.2004, http://clic-meeting.web.cern.ch/clic-meeting/2004/12_03min.html

[52] R. Corsini, D. Schulte, "Beam Transverse Stability in the CLIC Combiner Rings", CERN/PS 2002-072 and CLIC Note 539 (2002)

[53] D. Schulte, Private Communication

[54] H. Braun, R. Corsini (Ed.), T.E. D'Amico, J.P. Delahaye, G. Guignard, C.D. Johnson, A. Millich, P. Pearce, L. Rinolfi, A.J. Riche, R.D. Ruth, D. Schulte, L. Thorndahl, M. Valentini, I. Wilson, W. Wuensch, "The CLIC RF Power Source: a Novel Scheme of Two-Beam Acceleration for Electron-Positron Linear Colliders", CERN 99-06 (1999)

[55] E.T. D'Amico, G. Guignard, "First Order Design of a New Type of Isochronous Arc", CLIC Note 292 (1995)

[56] G. Carron, E. Jensen, M. Luong, A. Millich, E. Rugo, I. Syratchev, L. Thorndahl, "Design of a 3 GHz Accelerator Structure for the CLIC Test Facility (CTF3) Drive Beam", Linac 2000, TUA16, CLIC Note 451 (2000)

[57] E. Jensen, I. Syratchev, W. Wuensch, "Slotted-Iris Structure Studies", PAC 2001, MPPH040, CLIC Note 481 (2001)

[58] E. Jensen, "CLIC Drive Beam Accelerating Structures", LINAC 2002, CLIC Note 538 (2002)

[59] R. Corsini et al., "First Full Beam Loading Operation with the CTF3 Linac", EPAC 2004, CLIC Note 604 (2004)

[60] A. Yano, "Development of an L-band Multi-Beam Klystron", International Vacuum Electronics Conference, IVEC 2005